LETTER

doi:10.1038/nature13560

A shift of thermokarst lakes from carbon sources to sinks during the Holocene epoch

K. M. Walter Anthony[1], S. A. Zimov[2], G. Grosse[3]†, M. C. Jones[1,4], P. M. Anthony[1], F. S. Chapin III[5], J. C. Finlay[6], M. C. Mack[7], S. Davydov[2], P. Frenzel[8] & S. Frolking[9]

Thermokarst lakes formed across vast regions of Siberia and Alaska during the last deglaciation and are thought to be a net source of atmospheric methane and carbon dioxide during the Holocene epoch[1–4]. However, the same thermokarst lakes can also sequester carbon[5], and it remains uncertain whether carbon uptake by thermokarst lakes can offset their greenhouse gas emissions. Here we use field observations of Siberian permafrost exposures, radiocarbon dating and spatial analyses to quantify Holocene carbon stocks and fluxes in lake sediments overlying thawed Pleistocene-aged permafrost. We find that carbon accumulation in deep thermokarst-lake sediments since the last deglaciation is about 1.6 times larger than the mass of Pleistocene-aged permafrost carbon released as greenhouse gases when the lakes first formed. Although methane and carbon dioxide emissions following thaw lead to immediate radiative warming, carbon uptake in peat-rich sediments occurs over millennial timescales. We assess thermokarst-lake carbon feedbacks to climate with an atmospheric perturbation model and find that thermokarst basins switched from a net radiative warming to a net cooling climate effect about 5,000 years ago. High rates of Holocene carbon accumulation in 20 lake sediments (47 ± 10 grams of carbon per square metre per year; mean ± standard error) were driven by thermokarst erosion and deposition of terrestrial organic matter, by nutrient release from thawing permafrost that stimulated lake productivity and by slow decomposition in cold, anoxic lake bottoms. When lakes eventually drained, permafrost formation rapidly sequestered sediment carbon. Our estimate of about 160 petagrams of Holocene organic carbon in deep lake basins of Siberia and Alaska increases the circumpolar peat carbon pool estimate for permafrost regions by over 50 per cent (ref. 6). The carbon in perennially frozen drained lake sediments may become vulnerable to mineralization as permafrost disappears[7–9], potentially negating the climate stabilization provided by thermokarst lakes during the late Holocene.

Approximately 30% of global permafrost carbon is concentrated in 7% of the permafrost region (about 1.32 million km^2) in North Siberia, Alaska, and northwest Canada[6] (Extended Data Fig. 1). Here icy, organic-rich, silt-dominated sediments, termed yedoma, were deposited to an average depth of 25 m in unglaciated regions during the late Pleistocene glacial period[10]. The average organic carbon contents of frozen yedoma, typically 2%–5% (refs 5 and 11), are higher and more decomposable than in most thawed mineral soils because fresh organic inputs from the tundra–steppe ecosystem were buried and frozen into rapidly accumulating sediment[10].

During yedoma sedimentation, massive ice wedges grew as seasonal melt water migrated into frost cracks and refroze. When these ice wedges melt under the warmer Holocene climate, the ground subsides (thermokarst), forming deep lakes (10–30 m). Microbes decompose thawed yedoma organic matter in anaerobic lake bottoms, releasing methane, a potent greenhouse gas, which further accelerates permafrost thaw in a positive feedback cycle[1]. These deep, methane-emitting lakes expand until thaw creates a drainage channel. Partial lake drainage lowers lake water level, slowing thermokarst and stimulating growth of benthic mosses and other plants. When lakes drain completely, lakebed sediments, rich with the remains of moss and other organic matter, freeze and reform permafrost (Fig. 1).

Since the last deglaciation (the past 14.7 thousand years, kyr), about 70% of all yedoma area thawed beneath thermokarst lakes and streams (Methods). While thermokarst released a fraction of yedoma carbon to the atmosphere as greenhouse gases[2–4] and a lesser fraction to downstream export (Supplementary Information section 1.5), atmospheric carbon dioxide was absorbed by thermokarst basins through assimilation by contemporary plants. Plant remains are sequestered in newly formed Holocene*-aged permafrost of deep, drained thermokarst-lake basins (alases). Holocene* denotes the Holocene (11.7 kyr ago to present) and pre-Holocene deglacial (14–11.7 kyr ago) period of alas formation (Supplementary Information section 1.1). The extent to which carbon uptake by thermokarst lakes and alases offsets their greenhouse gas emissions has not been determined.

In this study we used field observations of Siberian permafrost exposures, radiocarbon dating, spatial analyses and modelling to (1) quantify the thermokarst-basin carbon stock and (2) document the role of thermokarst-lake carbon accumulation in compensating for greenhouse gas emissions from permafrost thaw in the Holocene.

At 49 widely dispersed steep-bluff sites (up to 25 m high) along rivers and coasts in North Siberian tundra and boreal forests, we quantified permafrost carbon pools in refrozen sediments of alases (Methods, Fig. 2). We compared alas carbon stocks, ^{14}C ages, and macrofossil composition to those of the adjacent undisturbed yedoma (up to 46 m high). We found that yedoma that thawed beneath lakes during the Holocene* and subsequently refroze when the lakes drained lost 28% ± 12% (mean ± standard error (s.e.), Extended Data Table 2) of its organic carbon to greenhouse gas production.

Basal dates compiled from alases in North Siberia, Alaska and northwest Canada (collectively called Beringia) indicate widespread thermokarst-lake formation around 14–9 kyr ago (Fig. 3a, Supplementary Table 2), generating a major northern source of atmospheric methane during deglaciation[2,4]. During subsequent millennia, mosses and other plants growing in and around lakes assimilated atmospheric carbon and were buried and preserved in lake sediments, mitigating the loss of permafrost-derived carbon from thermokarst lakes. Our conservative estimate for the mass of Holocene* organic carbon accumulation in Beringian alases (159 ± 24 Pg over 0.93 million km^2) is 1.6 times larger than the mass of Pleistocene-aged yedoma carbon that was released by methane and carbon dioxide production in thawed sediments beneath the same lakes (100 ± 34 Pg) (Fig. 3d; Extended Data Table 3). Additional methane generated from decomposition of Holocene* organic material was also emitted (Supplementary Information section 1.6.3).

[1]Water and Environmental Research Center, University of Alaska, Fairbanks, Alaska 99775-5860, USA. [2]Northeast Scientific Station, Pacific Institute for Geography, Far-East Branch, Russian Academy of Sciences, Cherskii 678830, Russia. [3]Geophysical Institute, University of Alaska, Fairbanks, Alaska 99775-7320, USA. [4]US Geological Survey, Reston, Virginia 20192, USA. [5]Institute of Arctic Biology, University of Alaska, Fairbanks, Alaska 99775-7000, USA. [6]Department of Ecology, Evolution and Behavior, University of Minnesota, Saint Paul, Minnesota 55108, USA. [7]Department of Biology, University of Florida, Gainesville, Florida 32611, USA. [8]Max Planck Institute for Terrestrial Microbiology, Marburg 35043, Germany. [9]Institute for the Study of Earth, Oceans, and Space, University of New Hampshire, Durham, New Hampshire 03824-3525, USA. †Present address: Alfred Wegener Institute Helmholtz Centre for Polar and Marine Research, Potsdam 14473, Germany.

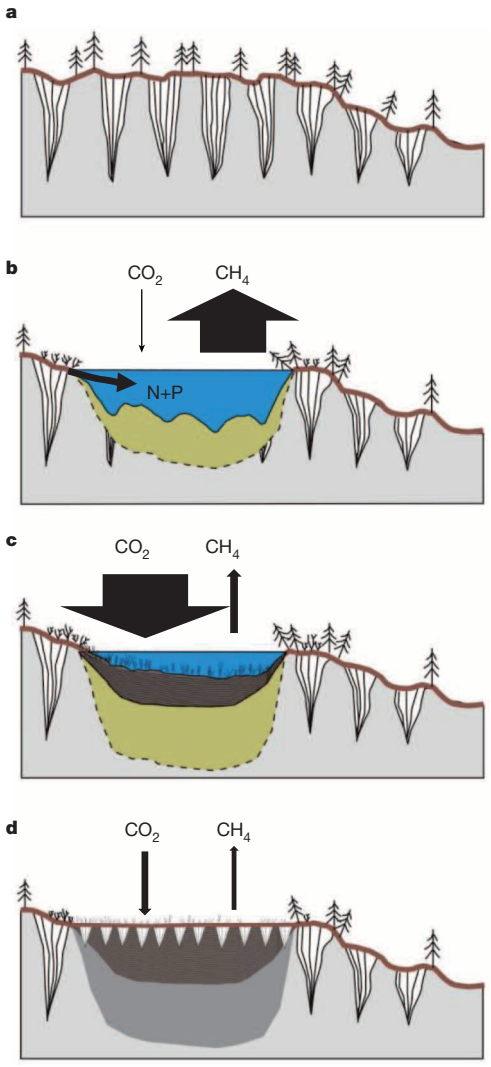

Figure 1 | Carbon cycling during the development of deep thermokarst lakes. **a**, Yedoma with massive Pleistocene ice wedges. **b**, Thermokarst-lake expansion (thaw bulb shown in yellow; thaw boundary shown as a dotted line) accompanied by Pleistocene-aged CH_4 emissions and release of N and P from yedoma into lakes, stimulating aquatic productivity and CO_2 uptake, which offset Pleistocene-aged CO_2 emissions from yedoma decay. **c**, Partially drained lake with atmospheric CO_2 uptake by plants forming thick Holocene* organic carbon deposits (brown) exceeding CH_4 emissions from contemporary organic matter decay. **d**, Refreezing of remaining Pleistocene and Holocene* carbon in sediments following complete lake drainage (new ice wedges are shown as triangles), with peatland-type CH_4 emissions and CO_2 uptake. The thicknesses of CH_4 and CO_2 arrows are scaled by relative magnitude on a carbon-mass basis (Supplementary Information section 1.6).

Since greenhouse gas emissions and carbon sequestration have counteractive effects on climate (warming versus cooling, respectively), the radiative impacts of both processes must be scaled for comparison. We developed simple deglacial-to-present thermokarst-basin carbon flux trajectories (Fig. 3b) based on estimates of contemporary methane flux (Supplementary Information section 1.6.3), total yedoma carbon lost as carbon dioxide and methane (100 ± 34 Pg), total accumulated Holocene* carbon (159 ± 24 Pg), and thermokarst-lake initiation dates. Flux trajectories were used as input to a simple atmospheric perturbation model developed originally to assess northern peatland carbon feedbacks to climate in the Holocene[12] (Extended Data Table 4). Thermokarst lakes caused a net climate warming of 0.06 ± 0.03 W m^{-2} at the peak of their formation during deglaciation (Fig. 3c), driven primarily by methane release from thawed, decaying yedoma. The peak climate impact of yedoma lakes was much larger than that of all northern peatlands in the early Holocene[12]. Owing to high carbon accumulation in existing basins and a slowdown of lake formation, thermokarst-lake impact on climate switched from net warming to net cooling about 5 kyr ago. Since that time these carbon-sequestering lake basins have caused an increasing net cooling to the present-day net radiative forcing of −0.06 ± 0.02 W m^{-2} (Fig. 3c).

Following drainage, the peat-rich sediments of these lake basins refroze, sequestering a large, Holocene* C pool in permafrost. This deep-lake carbon, now part of the terrestrial carbon stock, was not included in previous global carbon inventories because alas deposits had not been systematically sampled for this purpose[6,13]. Rather, past approaches assumed homogeneous yedoma carbon concentrations for deep frozen deposits in the region (Supplementary Information section 3.5). This newly recognized alas carbon pool (159 ± 24 Pg) is more than twice as large as the West Siberian Lowland peat-carbon stock (70 Pg; ref. 14) and increases the existing estimate of northern circumpolar permafrost-zone peatland carbon (277 Pg; ref. 6) by 56%.

Past syntheses have suggested that climatic controls limit carbon accumulation in lakes north of 62° N to less than 10 g m^{-2} yr^{-1} during the Holocene[15]. Radiocarbon dating of terrestrial plant macrofossils buried in our Siberian study-lake sediments revealed exceptional rates of long-term carbon accumulation (47 ± 10 g C m^{-2} yr^{-1}, mean ± s.e., $n = 20$ lakes). These rates are about 2.5-fold and 5-fold higher than the global averages for northern peatlands (18.6 g C m^{-2} yr^{-1}; ref. 16) and lakes (4.5–14 g C m^{-2} yr^{-1}; ref. 17) (Fig. 4), respectively. We found similarly high carbon accumulation (30–182 g C m^{-2} yr^{-1}) when we reconstructed published ^{14}C-dated alas profiles in other yedoma subregions; similar rates were also found in deep, arctic Alaska lakes (Supplementary Table 3).

We attribute the high carbon accumulations in our Siberian study lakes to: (1) thermokarst-related shore erosion and deposition of terrestrial organic matter in lake bottoms; (2) high aquatic productivity enhanced by nutrient supply from thawing yedoma; and (3) the unique preservation conditions in deep thermokarst lakes. In addition to the initial surface layer of organic soils slumping into lakes as topographic changes began, the productivity of terrestrial communities surrounding lakes increased when thermokarst lakes formed. We observed enhanced shrub growth along modern lake margins, probably resulting from the protected environment created by thaw subsidence (for example, enhanced snow accumulation and wind protection); deepening of the active layer, which mobilizes nutrients from thawed soils; and the concave shape of thermokarst features, which traps nutrient and water flow from the surrounding watershed[18]. As the lake margins expand, shrubs fall into the lakes.

Macrofossil analysis and ^{14}C dating of modern and palaeolake sediments indicated that upland plants, littoral sedges and benthic brown mosses contributed nearly equally to the macrofossil remains of the deep lake deposits (Fig. 2a); however, we observed the fastest rates of carbon accumulation (89 ± 15 g C m^{-2} yr^{-1}, mean ± s.e., $n = 8$, maximum 185 g C m^{-2} yr^{-1}) in sequences dominated by thick, *in situ*, benthic-moss peat (Supplementary Information section 3.2). Given their capacity to flourish under low temperature and light[19], brown mosses (Amblystegiaceae) are the dominant macrophyte in arctic lakes[20], including the North Siberian thermokarst lakes. We observed such mosses in all present-day yedoma lakes, but they were most prolific along floating mats in partially drained, yet still deep (8–12 m) boreal yedoma lakes. Aquatic mosses are particularly responsive to phosphorus fertilization[20,21] and nutrient release from permafrost thaw on lakeshores[22]. In our study region, thawing yedoma releases nitrogen and phosphorus (Supplementary Information section 1.8, Extended Data Table 5), leading to high hypolimnetic orthophosphate concentrations (mean 233 μg P per litre), and moss-tissue nitrogen (2.0 ± 0.22% dry weight) and phosphorus (0.12 ± 0.01% dry weight) concentrations above critical levels for moss growth[20]. Nutrient concentrations in North Siberian yedoma lakes were one to three orders of magnitude higher than in shallow, non-yedoma thermokarst lakes

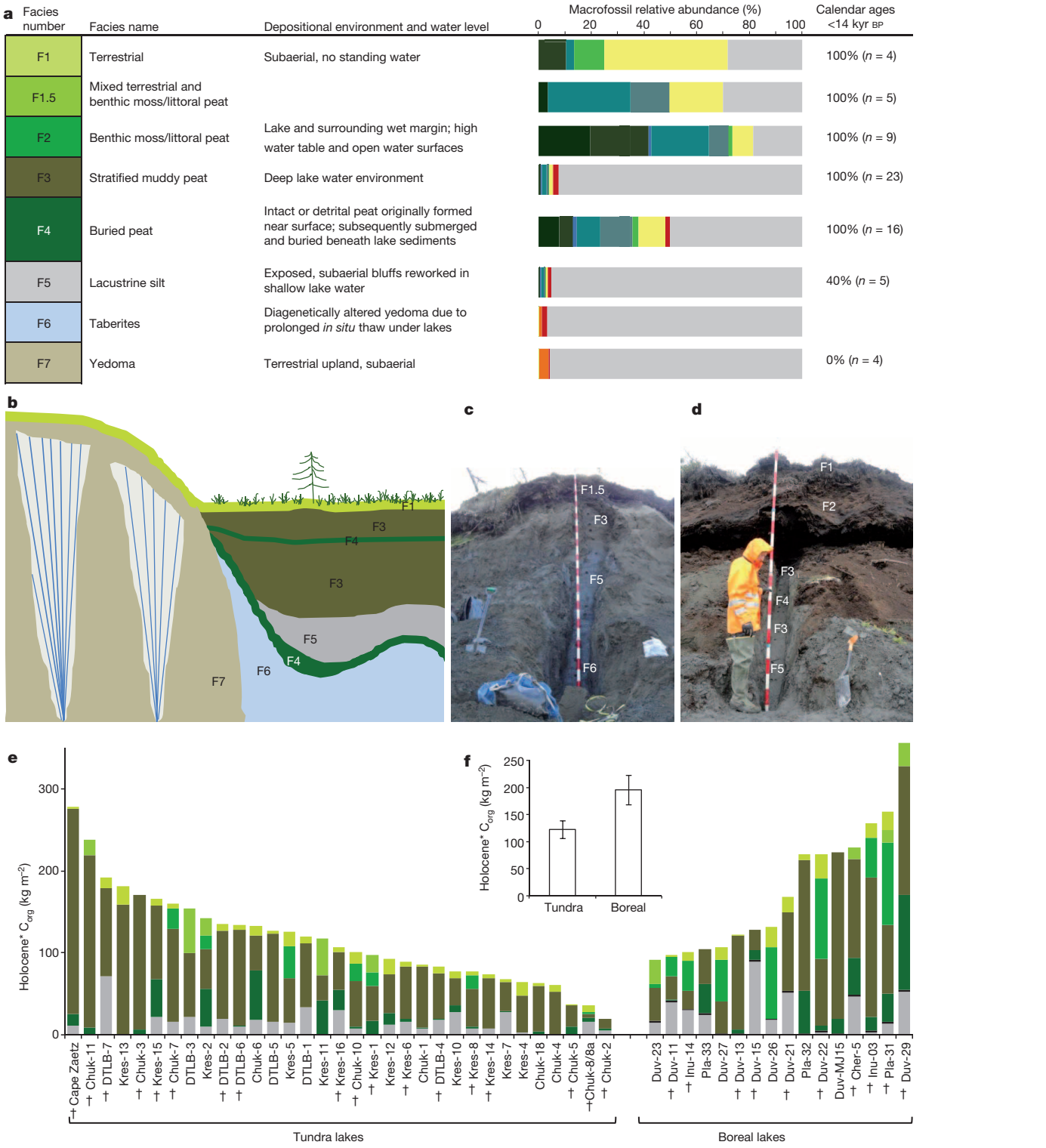

Figure 2 | Facies description and carbon contents in the deep thermokarst-lake landscape. **a**, Facies depositional environment; relative abundance of macrofossils (dark green, aquatic moss; mid-green, wet moss; light blue, other aquatic; turquoise, wet sedge; blue, other emergent mosses; light green, unidentified; yellow, terrestrial; orange, dry graminoid; red, detritus in silt; grey, inorganic) (Supplementary Table 1) scaled by the mean organic matter content of the facies; and fraction of macrofossils with ^{14}C ages <14 kyr ago in permafrost exposures (Extended Data Table 1). Facies were determined in the field based on physical properties; subsequent ^{14}C dating confirmed facies ages (Pleistocene versus Holocene*). The schematic (**b**) and photographs (**c**, **d**) show examples of facies in cross-section; pole marks are 20 cm. Coloured bars in **e** indicate Holocene* organic carbon stocks by facies observed in 49 refrozen, thermokarst exposures (see **a**; black, wood; dagger, fully exposed). **f**, Boreal-zone thermokarst basins accumulated more Holocene* organic carbon (mean ± s.e.; 196 ± 27 kg C m^{-2}, $n = 10$) than tundra basins (122 ± 16 kg C m^{-2}, $n = 18$; one-sided t-test, $P < 0.05$).

in the same study region (Extended Data Fig. 3) and deep, non-yedoma lakes in Alaska (Extended Data Fig. 4), where mosses are less abundant[23].

Cold and anoxic conditions fostering organic matter preservation[7,8] also lead to high sediment carbon accumulation. Strong stratification resulting from high solute concentrations[24] (indicated by high specific

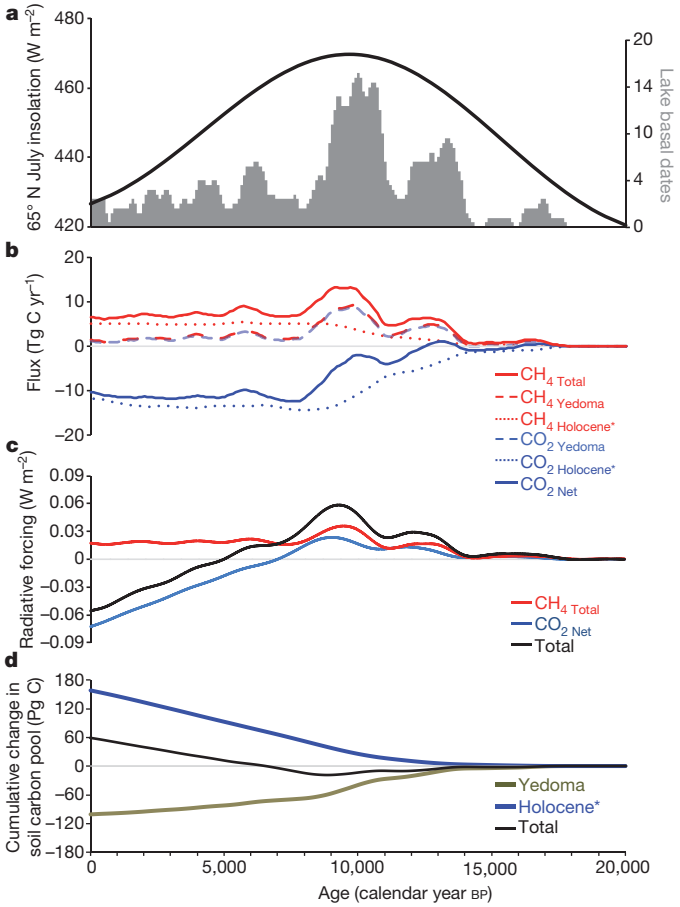

Figure 3 | Thermokarst-lake carbon cycling dynamic since the last deglaciation. **a**, The increase in arctic insolation[30] coincided with widespread thermokarst-lake formation during deglaciation (Supplementary Information section 1.6.1, Supplementary Table 2). **b**, Carbon flux trajectories for yedoma-region thermokarst basins determined by basal date frequency in **a** (CO_2-C (the carbon component of carbon dioxide) uptake by peat formation, negative flux; CO_2-C emission from thawed yedoma decay and CH_4-C (the carbon component of methane) emissions, positive flux). The solid red line in **b** is the sum of CH_4-C emissions from decay of thawed yedoma deposits (dashes) and younger organic matter termed Holocene* (Supplementary Information section 1.1) in thermokarst basins (dots). Identical yedoma-derived CH_4-C and CO_2-C emission curves are based on methanogenesis stoichiometry (Supplementary Information section 1.6.2). **c**, Radiative forcing due to atmospheric perturbations in CH_4 and CO_2 concentration for flux trajectories shown in **b**. **d**, Cumulative changes in the yedoma-region permafrost carbon pool due to loss of yedoma carbon to the atmosphere by thermokarst-lake formation (negative) and atmospheric carbon uptake and burial by the same lakes (positive). See Supplementary Information section 1.6 and Extended Data Table 3 for detailed methods and uncertainties.

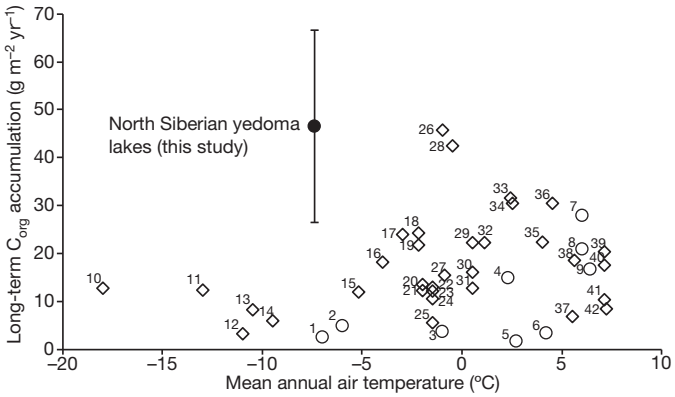

Figure 4 | Comparison of long-term organic carbon accumulation rates among northern lakes and peatlands by mean annual temperature. Despite cold temperatures in the North Siberia yedoma region, thermokarst lakes there (closed circle, mean and 95% confidence interval) accumulated organic carbon faster than other northern lakes (open circles labelled 1–9) and peatlands (open diamonds labelled 10–42; except the West Siberian Lowlands, labelled 26 and 28), 228 European lakes (5.6 g m^{-2} yr^{-1}; ref. 15) and global lakes (4.5–14 g m^{-2} yr^{-1}; ref. 17). See Supplementary Information section 3.1 for regional data references.

conductivity and dissolved organic carbon; Extended Data Figs 3 and 4), protection from wind mixing by steep banks and small surface-area to volume ratios, and proximity to permafrost maintained unusually cold lake bottom temperatures (down to 1.5 °C year round). When lakes drain completely, sediment organic matter rapidly freezes (on a time-scale of decades)[25], stabilizing this carbon in permafrost.

Permafrost temperatures are increasing in Siberia, as in most of the Arctic[26]. Global annual air temperature increases as little as 1.5 °C, less than the projected 1.9 °C–3.7 °C air temperature increase by 2100 AD[27], should lead to pronounced reductions in permafrost stability[28]. Our results suggest that if new, deep thermokarst lakes continue to form by localized permafrost thaw, then primary productivity and sedimentation in lakes, particularly tundra lakes where aquatic productivity is expected to increase (Supplementary Information section 3.3), will compensate for greenhouse emissions over millennial timescales if a permafrost-forming climate persists in the region.

Thermokarst lakes depend on permafrost for an impermeable base that constrains water drainage[29]. Widespread permafrost loss, predicted as early as 2100 in some yedoma subregions[9,27], will ultimately result in reduced lake and wetland abundance caused by drainage and drying[8], facilitating rapid sediment carbon decomposition[7]. Even partial mineralization of the alas carbon pool, together with the surrounding Pleistocene-yedoma carbon that remains (all together about 450 Pg C; Extended Data Fig. 5 and Extended Data Table 3) may reverse the important role that thermokarst lakes have had in stabilizing climate for the past 5,000 years.

METHODS SUMMARY

In the field we described 49 drained, refrozen thermokarst-basin (alas) profiles and six yedoma profiles exposed along rivers and coasts in the North Siberian yedoma region (Extended Data Fig. 1). At each site we collected samples and measured the vertical distribution and cumulative thickness of individual stratigraphic facies F1–F7 (Fig. 2a and Extended Data Fig. 2, Supplementary Information section 1.3). Exposure thickness averaged 5.8 m in alases (range 1.25–20 m; Extended Data Table 1) and 31.5 m (range 14–40 m) in yedoma. From stratigraphy and our understanding of geomorphologic and palaeoenvironmental processes associated with the facies, we calculated the Pleistocene and Holocene* carbon accumulated in each profile using three independent approaches: (1) macrofossils (Fig. 2 and Supplementary Table 1), (2) radiocarbon dates (Fig. 2), and (3) carbon mass-balance equations (Supplementary Information section 1.4).

We estimated the yedoma carbon stock (325 ± 69 kg C m^{-2}) as the product of the mean yedoma organic carbon bulk density (26.0 ± 1.5 kg C m^{-3}) measured in eight subregions between the Kolyma Lowlands and Laptev Sea by us in this study (Extended Data Table 2) and ref. 5, an ice wedge volume of 50% ± 3% (refs 10 and 11), and an average deposit thickness of 25 ± 5 m based on broader regional estimates (Extended Data Tables 1 and 3). We calculated Holocene* carbon stocks in 49 individual refrozen thermokarst exposures as the sum of products of organic carbon bulk density and thickness measured for facies F1–F5 minus Holocene ice-wedge volume (10% of the 2-m surface layer) (Fig. 2e).

The deep, thermokarst-lake carbon pool estimate (159 ± 24 Pg) is the tundra/boreal area-weighted average Holocene* carbon stock measured in 28 fully exposed, refrozen thermokarst study sites (172 ± 19 kg C m^{-2}; Fig. 2f) extrapolated to the spatial extent of deep thermokarst-lake basins and thermoerosional gullies in the region (925,400 ± 93,000 km^2) (Extended Data Table 3). Assumptions, uncertainty analysis, and detailed methodology are described in the online-only Methods and the Supplementary Methods.

Online Content Methods, along with any additional Extended Data display items and Source Data, are available in the online version of the paper; references unique to these sections appear only in the online paper.

Received 13 July 2013; accepted 2 June 2014.
Published online 16 July 2014.

1. Walter, K. M., Zimov, S. A., Chanton, J. P., Verbyla, D. & Chapin, F. S., III. Methane bubbling from Siberian thaw lakes as a positive feedback to climate warming. *Nature* **443,** 71–75 (2006).
2. Walter, K. M., Edwards, M. E., Grosse, G., Zimov, S. A. & Chapin, F. S. III. Thermokarst lakes as a source of atmospheric CH_4 during the last deglaciation. *Science* **318,** 633–636 (2007).
3. Petrenko, V. V. *et al.* $^{14}CH_4$ measurements in Greenland ice: investigating last glacial termination CH_4 sources. *Science* **324,** 506–508 (2009).
4. Brosius, L. S. *et al.* Using the deuterium isotope composition of permafrost meltwater to constrain thermokarst lake contributions to atmospheric CH_4 during the last deglaciation. *J. Geophys. Res.* **117,** G01022 (2012).
5. Schirrmeister, L. *et al.* Fossil organic matter characteristics in permafrost deposits of the northeast Siberian Arctic. *J. Geophys. Res.* **116,** G00M02 (2011).
6. Tarnocai, C. *et al.* Soil organic carbon pools in the northern circumpolar permafrost region. *Glob. Biogeochem. Cycles* **23,** GB2023 (2009).
7. Maltby, E. & Immirzi, P. Carbon dynamics in peatlands and other wetland soils: regional and global perspectives. *Chemosphere* **27,** 999–1023 (1993).
8. Avis, C. A., Weaver, A. J. & Meissner, K. J. Reduction in areal extent of high-latitude wetlands in response to permafrost thaw. *Nature Geosci.* **4,** 444–448 (2011).
9. Slater, A. G. & Lawrence, D. M. Diagnosing present and future permafrost from climate models. *J. Clim.* **26,** 5608–5623 (2013).
10. Zimov, S. A., Schuur, E. A. G. & Chapin, F. S. Permafrost and the global carbon budget. *Science* **312,** 1612–1613 (2006).
11. Strauss, J. *et al.* The deep permafrost carbon pool of the Yedoma region in Siberia and Alaska. *Geophys. Res. Lett.* **40,** 6165–6170 (2013).
12. Frolking, S. & Roulet, N. T. Holocene radiative forcing impact of northern peatland carbon accumulation and methane emissions. *Glob. Change Biol.* **13,** 1079–1088 (2007).
13. Hugelius, G. *et al.* The Northern Circumpolar Soil Carbon Database: spatially distributed datasets of soil coverage and soil carbon storage in the northern permafrost regions. *Earth Syst. Sci. Data* **5,** 3–13 (2013).
14. Smith, L. C. *et al.* Siberian peatlands a net carbon sink and global methane source since the early Holocene. *Science* **303,** 353–356 (2004).
15. Kastowski, M., Hinderer, M. & Vecsei, A. Long-term carbon burial in European lakes: Analysis and estimate. *Glob. Biogeochem. Cycles* **25,** GB3019 (2011).
16. Yu, Z., Beilman, D. W. & Jones, M. C. in *Carbon Cycling in Northern Peatlands* (eds Baird, A. J., Belyea, L. R., Comas, X., Reeve, A. S. & Slater, L. D.) Geophysical Monograph Series 184 (AGU, 2009).
17. Tranvik, L. J. *et al.* Lakes and reservoirs as regulators of carbon cycling and climate. *Limnol. Oceanogr.* **54,** 2298–2314 (2009).
18. Lantz, T. C., Kokelj, S. V., Gergel, S. E. & Henry, G. H. R. Relative impacts of disturbance and temperature: persistent long-term changes in microenvironment and vegetation in retrogressive thaw slumps. *Glob. Change Biol.* **15,** 1664–1675 (2009).
19. Welch, H. E. & Kalff, J. Benthic photosynthesis and respiration in Char Lake. *J. Fish. Res. Board Can.* **31,** 609–620 (1974).
20. Riis, T., Olesen, B., Katborg, C. K. & Christoffersen, K. S. Growth rate of an aquatic bryophyte (*Warnstorfia fluitans* (Hedw.) Loeske) from a high arctic lake: effect of nutrient concentration. *Arctic* **63,** 100–106 (2010).
21. Bowden, W. B., Finlay, J. C. & Maloney, P. E. Long-term effects of PO_4 fertilization on the distribution of bryophytes in an arctic stream. *Freshwat. Biol.* **32,** 445–454 (1994).
22. Mesquita, P. S., Wrona, F. J. & Prowse, T. D. Effects of retrogressive permafrost thaw slumping on sediment chemistry and submerged macrophytes in Arctic tundra lakes. *Freshwat. Biol.* **55,** 2347–2358 (2010).
23. Hershey, A. Effects of predatory sculpin on the chironomid communities in an arctic lake. *Ecology* **66,** 1131–1138 (1985).
24. Houser, N. J. Water color affects the stratification, surface temperature, heat content, and mean epilimnetic irradiance of small lakes. *Can. J. Fish. Aquat. Sci.* **63,** 2447–2455 (2006).
25. Jones, B. M. *et al.* Modern thermokarst lake dynamics in the continuous permafrost zone, northern Seward Peninsula, Alaska. *J. Geophys. Res.* **116,** G00M03 (2011).
26. Romanovsky, V. E. *et al.* Thermal state of permafrost in Russia. *Permafrost Periglacial Process.* **21,** 136–155 (2010).
27. Stocker, T. F. *et al.* Technical summary. In *Climate Change 2013: The Physical Science Basis. Contribution of Working Group I to the Fifth Assessment Report of the Intergovernmental Panel on Climate Change* (eds Stocker, T. F. *et al.*) (Cambridge Univ. Press, 2014).
28. Vaks, A. *et al.* Speleothems reveal 500,000-year history of Siberian permafrost. *Science* **340,** 183–186 (2013).
29. Smith, L. C., Sheng, Y. & MacDonald, G. M. A first pan-Arctic assessment of the influence of glaciation, permafrost, topography and peatlands on northern hemisphere lake distribution. *Permafrost Periglacial Process.* **18,** 201–208 (2007).
30. Berger, A. & Loutre, M. F. Insolation values for the climate of the last 10 million years. *Quat. Sci. Rev.* **10,** 297–317 (1991).

Supplementary Information is available in the online version of the paper.

Acknowledgements We thank L. Brosius, K. Davies, L. Farquharson, J. Neff and N. Zimov for assistance with field and laboratory work; G. Kling for p_{CO_2} and DOC data sets for Lake N1 (Alaska); and E. A. G. Schuur, B. Gaglioti, C. Bernhardt and S. Neuzil for constructive comments on the manuscript. Research funding was provided by the NSF (OPP-0099113, OPP-0732735 and ARC-1304823) and NASA (NNX08AJ37G). Additional support was received from other NSF projects (OPP-1107892, OPP-6737545, PLR-1303940), the USGS, the DOE (DE-SC0010580) and ERC number 338335.

Author Contributions K.M.W.A. had primary responsibility for study design, field work, laboratory measurements, data analysis, interpretation and writing. S.A.Z. co-designed the study and contributed substantially to data interpretation. M.C.J., G.G., P.M.A. and F.S.C. contributed to project planning, field and laboratory work, and interpretation of results. M.C.J. provided expertise in macrofossil identification. G.G. conducted spatial analyses. K.M.W.A., M.C.M., J.C.F. and S.D. conducted laboratory analyses of lake water samples and ice wedges, and designed and implemented the component of terrestrial vegetation and soil nutrient cycling. P.F. conducted anaerobic laboratory incubations. S.F. created the atmospheric model for radiative forcing calculations. All authors contributed to the revision and integration of the manuscript.

Author Information Reprints and permissions information is available at www.nature.com/reprints. The authors declare no competing financial interests. Readers are welcome to comment on the online version of the paper. Correspondence and requests for materials should be addressed to K.M.W.A. (kmwalteranthony@alaska.edu).

METHODS

Permafrost alas and yedoma exposures. Thermokarst profiles represented refrozen lake-sediment sequences and overlying drained-lake basin soils (alases) at all sites, except Duv-26, which was a thermoerosional gully associated with a former stream. Fieldwork was conducted in August (of 2009 and 2011), when seasonal thaw is greatest. At each study outcrop we removed seasonally thawed sediment with shovels to expose permafrost in cross-section along a vertical profile (Fig. 2). We studied exposures with the steepest bluff angles to avoid locations where permafrost may have thawed, slumped and re-frozen since formation. Bluff angle was a function of present-day erosion dynamics along rivers and coasts into the palaeolake sediment sequences; it was not a function of location in lake basins. Detailed mapping of lake bed morphology in modern yedoma thermokarst lakes[31] and palaeolakes (this study) has revealed that these lake beds are not flat, with the exception of old or large lakes where erosion and sedimentation have partially worn down baydjarakhs (thermokarst mounds) and completely filled in thermokarst depressions. Relatively high relief in actively expanding yedoma thermokarst occurs at the basin scale, but also at the finer scale of the former ice-wedge network (approximately 10–12 m)[32–34]. At the basin scale, yedoma thermokarst lakes have steep bluffs (often >10 m), particularly along expanding thermokarst margins where ground ice rapidly melts, leading to subsidence and high relief. At a finer scale, the bottom of an actively expanding thermokarst lake has a morphology similar to an egg carton, with micro-relief among baydjarakhs often exceeding 1 m. In contrast to core drilling and sampling, studying permafrost exposures has the advantage of providing a broader perspective on the distribution of sedimentary facies because it is possible to visually trace horizons identified in exposures across lake basins. In palaeolakes, we often saw the undulating pattern of baydjarakhs at the base of the sedimentary sequence, which later formed a flatter surface across basins as lakes matured and filled in with peat-rich sediments (Fig. 1).

The use of a single sampling location in lake basins with strong sediment focusing (accumulation of fine particles in deep parts of a lake basin) has the potential to lead to false conclusions about climate-driven sediment deposition dynamics and inflated carbon accumulation rates if sedimentation rates are improperly scaled. Multiple, distributed cores, geophysical methods for cross-basin scaling of sedimentation, and focusing-corrected carbon burial rates have been used to avoid such false conclusions[35–37]. Since the bluffs we studied were located at various, non-uniform positions within basins (that is, not always in the lake centre or at sites with a particular deposit thickness), there was no bias in our sampling towards environments of sediment focusing. This also implies that among the sets of boreal and tundra exposures we studied, various depositional environments in the former lakes (that is, near-shore, transitional, and pelagic zones) are represented.

With shovels we exposed cross-sections of Holocene and Pleistocene deposits from the ground surface down to depths ranging from 1.25 m to 20 m below the surface in the 49 alas sites (exposure depth: mean 5.6 m, median 4.8 m, range 1.25–20 m; Extended Data Table 1). Among the 28 exposures where we had high confidence that we had dug close to the base of the Holocene* deposits, the mean thickness of sediments containing Holocene* carbon was 5.8 m (median 5.0 m). Average alas bluff height, including uncovered deposits beneath our study exposures, was 13 ± 1 m (s.e.), $n = 49$. Our map-based analysis of undisturbed yedoma deposit thickness surrounding the alas exposures yielded 38 ± 2 m (s.e.), $n = 17$.

At each alas exposure site we measured the vertical distribution and cumulative thickness of each of facies F1–F6 (Supplementary Information section 1.3). In a subset of nine alases we measured the thickness of surface peat deposits along cross-basin transects with 5 to 15 measurement sites per basin. We found that the basin mean peat thicknesses were not statistically different from the point measurements at single exposures (Wilcoxon signed rank test, $P = 0.6$). This demonstrates that there was no bias in our field sampling locations.

In addition to alases, we sampled yedoma (F7) profiles representing the Pleistocene permafrost of non-thermokarst surfaces in each of the North Siberia study regions, except Krestovskiy Cape (Extended Data Fig. 1). The sampling depths of yedoma ranged from 1.5 m to 37 m below the ground surface. Yedoma exposure thickness averaged 31.5 m (range 14–40 m). We did not sample the Holocene carbon content of soils overlying the undisturbed Pleistocene-aged yedoma deposits.

After carefully cleaning study exposures with spatulas, we characterized the cryolithology, differentiated the facies, and collected 595 soil samples (up to 39 samples per vertical profile) for laboratory analyses. In 2009, we chipped 212 frozen samples (0.3–0.5 kg) from exposures with hatchets and hammers. In 2011 we used a 75-cm^3 hole-saw mounted on a hand-held hammer drill to collect 383 samples of known volume for dry bulk density determination. To our knowledge, this constitutes the largest data set of yedoma-region permafrost samples from which population-level organic carbon bulk density could be calculated on the basis of the products of bulk density and organic matter content measured on the same samples. Alas samples were collected as one individual sample per depth; 2011 yedoma (F7) samples were usually collected in triplicate. Analytical results of triplicate samples were averaged to avoid pseudo-replication in statistical analyses. We estimated gravimetric ice content of permafrost samples as weight loss after drying at 105 °C to constant weight, expressed as a percentage of fresh weight (wt%). We determined the soil moisture of thawed, active layer samples in alases using the same method. We determined organic and inorganic matter contents of all samples after oven drying by loss-on-ignition at 550 °C and 950 °C for two hours, respectively[38]. On a subset of 63 samples we determined total organic carbon as the difference between total carbon using a Leco CHN analyser and the inorganic carbon component using titration[39]. We estimated organic carbon concentrations in the remainder of the samples based on the relationship between loss-on-ignition (percentage organic matter, P_{om}) and organic carbon concentration (P_{oc}) as follows: $P_{oc} = 0.5544 \times P_{om}$ ($P < 0.0001$; $r^2 = 0.9969$). The organic carbon bulk density (in units of kg C m^{-3}) was calculated as dry bulk density multiplied by percent organic carbon on a per sample basis.

We characterized macrofossil assemblages on 225 field samples collected in alas and yedoma exposures (Supplementary Information section 1.2, Supplementary Table 1). From stratigraphy and our understanding of geomorphologic and palaeoenvironmental processes associated with the facies (Supplementary Information section 1.3), we calculated the Pleistocene and Holocene* carbon accumulated in each profile using three independent approaches: (1) macrofossil assemblages (Fig. 2, Supplementary Table 1), (2) radiocarbon dates (Fig. 2), and (3) carbon mass-balance equations (Supplementary Information section 1.4). We refer to organic matter fixed via photosynthesis in and around the thermokarst basins as 'Holocene*' because the majority (93%) accumulated from 11.7 kyr ago to present (Fig. 3d); however, it should be noted that 7% of the non-yedoma, peat-rich carbon pool indicated by 'Holocene*' actually accumulated in thermokarst basins that formed before the Holocene during the deglacial warming between 14 kyr ago and 11.7 kyr ago. This follows terminology common to peatland studies[12,14]. Without the asterisk, Holocene refers to the period of 11.7 kyr ago to present.

Radiocarbon dating. We obtained accelerator mass spectrometry (AMS) radiocarbon dates on plant macrofossils picked from permafrost exposures and present-day lake sediment cores. Samples were analysed at the W. M. Keck Carbon Cycle AMS Laboratory or at the National Ocean Sciences AMS Facility (Supplementary Tables 2 and 3). All radiocarbon ages were calibrated to calendar ($\pm 2\sigma$) years before present (BP) using Calib 6.0 software (ref. 40).

Yedoma and thermokarst basin areas. We calculated the original Last Glacial Maximum extent of the core yedoma region in land areas exposed today in Beringia (1,322,000 km^2) using general maps of yedoma distribution in North and East Siberia (1,141,000 km^2) (ref. 41) and a surface geological map of Alaska that shows ice-rich silty deposits (181,000 km^2) (ref. 42), which we classify as yedoma. Based on literature data[43–47] and a new assessment of yedoma spatial continuity using high-resolution Siberian geological maps[48], we estimated the fraction of areas with degraded yedoma (about 70%; 925,400 km^2) within the original yedoma region land areas, including deep thermokarst-lake basins (50%–60%) and streams and rivers (about 10%–20%), as well as the remaining 30% of undisturbed yedoma that had not degraded since the Pleistocene. Deep thermokarst-lake basins include both present-day lakes as well as drained, refrozen lake basins. Landforms shaped by melting ground ice and fluvial erosion of streams and small rivers are known as 'thermoerosional gullies'. In our calculations we do not include known but smaller yedoma occurrences in valleys of the Yukon Territories (Canada) and Chukotka and Taymyr peninsulas (Russia).

To estimate the current ratio of yedoma located in tundra and boreal forest regions, we used the Circum Arctic Vegetation Map[49] to determine the yedoma-region extent in these two ecoregion categories. We calculated that 32% of the yedoma region is located in today's tundra regions (424,000 km^2) and 68% is located in boreal forest regions (898,000 km^2). Supplementary Information section 1.7.3 provides an uncertainty analysis of the geospatial analysis.

Pleistocene and Holocene carbon stocks and pool sizes. Parameters for calculating the Pleistocene and Holocene* carbon stocks and pool sizes are shown in Extended Data Tables 2 and 3a. The uncertainty analysis is summarized in Extended Data Table 3b and described in detail in Supplementary Information section 1.7.

We estimated the yedoma carbon stock (325 ± 69 kg C m^{-2}) as the product of the mean yedoma organic carbon bulk density (26.0 ± 1.5 kg C m^{-3}), measured in eight subregions between the Kolyma Lowlands and Laptev Sea by us in this study (Extended Data Table 2) and ref. 5, an average yedoma facies thickness of 25 ± 5 m, as determined from extensive literature[10,32,50–56], and an ice-wedge volume of $50 \pm 3\%$ (refs 10, 11, 32, 56). The error value of 3% is the approximate standard error of the mean ice wedge volume determined from careful measurements of ten sites[11]: 48% mean, 52% median, $n = 10$, min 35%, max 60%.

We estimated the Pleistocene carbon pool size for the 1.32 million km^2 yedoma territory of mainland Beringia (excluding continental shelves) at the Last Glacial Maximum (429 ± 101 Pg C) by applying the yedoma carbon stock (325 ± 69 kg C m^{-2}) to this area before extensive thermokarst activity occurred and propagating uncertainty associated with mean estimates of carbon bulk density (Extended Data Table

2), yedoma extent (Supplementary Information section 1.7.3), yedoma thickness and ice-wedge volume (Extended Data Table 3). Today the Pleistocene carbon pool size is 34% lower (284 ± 40 Pg C), since 70% of the original Last Glacial Maximum yedoma (area and volume) was degraded by thermokarst processes during the Holocene* and partially eroded by rivers (Supplementary Information section 1.5) or decomposed by microbes living in and beneath water bodies. The present-day Pleistocene carbon pool (284 ± 40 Pg C) is the sum of: (1) the remaining undisturbed yedoma (129 ± 30 Pg C), (2) thawed or previously thawed yedoma in thermokarst-lake basins (141 ± 26 Pg); and (3) thawed or previously thawed yedoma in the beds of thermokarst streams and rivers (14 ± 2 Pg) (Extended Data Table 3).

Upscaling calculations of the Holocene* carbon pool in thermokarst basins is based on the means of individual thermokarst exposure carbon stocks measured in tundra and boreal regions (Fig. 2e). We determined the Holocene* organic carbon stock of each thermokarst study exposure (in units of kg C m^{-2}; Fig. 2e) as the product of the Holocene* organic-carbon bulk density, measured on individual samples, and facies thickness in each exposure minus Holocene ice-wedge volume (10% of the 2-m surface layer). In instances where the thickness of a facies was measured in an exposure, but no representative samples collected, we applied the mean carbon bulk density for that facies calculated from all measured samples (Extended Data Table 1).

The deep, thermokarst-lake carbon pool estimate (159 ± 24 Pg) is the tundra/boreal area-weighted average Holocene* carbon stock measured in 28 fully exposed, refrozen thermokarst study sites (172 ± 19 kg C m^{-2}; Fig. 2f and Extended Data 2) extrapolated to the spatial extent of deep thermokarst-lake basins and thermoerosional gullies in the region (925,400 ± 93,000 km^2). This upscaling assumes that the 28 fully-excavated exposures represent the population of deep thermokarst-lake basin and thermoerosional gully environments in the yedoma region of Beringia (Fig. 2). The carbon stock data for the 28 exposures was normally distributed; a similar carbon accumulation was estimated for alases in other yedoma subregions (Supplementary Table 3). Extended Data Table 3 details our calculations and shows that upscaling based on median carbon stock values (104 kg C m^{-2} tundra, 195 kg C m^{-2} boreal) instead of mean values would result in a 4% difference in the landscape-scale estimate. We included thermoerosional gullies in our spatial extrapolation of Holocene* carbon deposits because we documented that the Holocene carbon accumulation in the thermoerosional gully Duv-26 was similar to that of the deep thermokarst lakes (Fig. 2e). Similar Holocene peat accumulations on top of thawed yedoma deposits have also been observed in thermoerosional gullies in other subregions of yedoma (for example, Laptev Sea)[57–59]. Additional thermokarst lakes formed in extensive, but thinner, yedoma deposits on the flanks of higher-relief topography and on previously exposed continental shelves. These thermokarst sites would increase the Holocene* carbon-stock estimates for thermokarst and their forcing effect on atmospheric carbon dioxide through time, but are not included in the calculations, which are therefore conservative. Our estimate of the thermokarst carbon pool is conservative for additional reasons, which are described in detail in Supplementary Information section 1.7.4.

Radiative forcing impact of deep thermokarst-lake carbon fluxes. We adapted the five-box atmospheric carbon dioxide and one-box atmospheric methane model established for northern peatlands[12] (Extended Data Table 4) to derive the net radiative effect of deep thermokarst basins from the onset of their formation during deglacial warming to the present (Fig. 3). Calculation of radiative forcing due to perturbations to the atmospheric carbon dioxide and methane budgets requires estimates of flux trajectories, which are a function of thermokarst-lake basin extent and flux rates. The extent of thermokarst basins across the landscape, which increased from the onset of deglaciation to the present, was assessed through evaluation of initiation or basal dates. Flux rates, which probably varied throughout the Holocene, were evaluated on the basis of time since basin initiation. Fluxes include methane and carbon dioxide emissions and the uptake of atmospheric carbon dioxide, resulting in carbon accumulation in lake sediments and peat. Methane emissions originated from two sources: thaw and decay of organic matter in yedoma permafrost and decomposition of younger organic matter fixed by photosynthesis in and around basins contemporary with thermokarst-lake cycling during deglaciation and the Holocene. Detailed methods, assumptions, and uncertainty assessment are provided in Supplementary Information section 1.6.

Modern lake sediments and mosses. Modern ecosystems provide a valuable, mechanistic understanding of alas deposit formation including their high carbon accumulation, high nutrient concentrations, and thriving benthic mosses in the lakes. From eight present-day yedoma lakes near Cherskii we extracted 21 sediment cores (49–210 cm) in 6.6-cm-diameter polycarbonate tubes using a piston hammer corer (Aquatic Instruments). Cores were extracted in the laboratory, visually described, and subsampled for quantification of dry bulk density and organic carbon and nitrogen. Terrestrial plant macrofossils from a subset of cores were radiocarbon dated (Supplementary Table 3). Modern benthic brown mosses sampled from present-day lakes were oven dried at 65 °C, ground through a Wiley Mill grinder (30 mesh), and redried at 65 °C before determination of carbon and nitrogen concentrations on a LECO Truspec CHN analyser. Phosphorus was measured on a 300XL ICP following digestion in a solution of nitric acid and perchloric acid (Extended Data Table 5).

In the mineral-dominated sediments of lake cores (and alas permafrost exposures) we frequently observed nonapatite inorganic phosphorus macrofossils in the form of vivianite; however, we did not quantify vivianite concentrations.

Limnology. To compare the physiochemical characteristics of yedoma thermokarst lakes versus other types of arctic lakes we sampled yedoma and non-yedoma thermokarst lakes in North Siberia and compared results to non-yedoma lakes in Alaska (ref. 60 and G. Kling, personal communication, 10 April 2013) and the pan-Arctic[61]. During June, July and August 2002–2003 we sampled nine thermokarst lakes formed in Pleistocene-aged yedoma permafrost near Cherskii and 13 thermokarst lakes formed in Holocene-aged deposits on the adjacent Kolyma River floodplain. Three yedoma lakes were sampled biweekly during summer. Owing to the limited depth of Holocene ice wedges, floodplain thermokarst lakes were shallow (1–2.5 m). Yedoma lakes, formed by melt of deep, Pleistocene ice wedges and high intrasedimentary ground ice content, ranged in depth from 6 m to 17 m.

At the deepest known location in each lake, we collected water column physiochemical parameters along a water-column depth profile. We measured temperature, dissolved oxygen, pH, redox, salinity and specific conductivity using a handheld Quanta Hydrolab Multiparameter Sonde (Hach Hydrometer). Bulk water samples were collected from various depths, filtered through Whatman GF/C glass microfibre filters, and analysed for orthophosphate (PO_4^{3-}, also expressed as soluble reactive phosphorus, SRP), nitrate (NO_3^-) and ammonium (NH_4^+) on a colorimetric autoanalyser (Astoria-Pacific) at the University of Florida. Ions were analysed using Astoria-Pacific method 305-A023-A00 for low-concentration ammonium, method 305-A173-A01 for low-concentration nitrite–nitrate, and method 305-A203-A00 for low-concentration orthophosphate. We measured dissolved organic carbon (DOC) at the University of Minnesota via high temperature combustion (Shimadzu). Chlorophyll-*a* was measured throughout the lake water column with a SCUFA Submersible Fluorometer (Turner Designs). We measured underwater photosynthetic active radiation (PAR, 400–700 nm) using an underwater spherical quantum sensor (LI-COR LI-193; LI-COR Biosciences) along the depth profiles to calculate irradiance following Wetzel and Likens[62]. The two-sided Mann–Whitney test was used to test differences in physiochemical parameters between the bottom water of North Siberian yedoma and floodplain lakes. Statistical analyses were performed in R[63].

Surface water temperature near the centres of five tundra yedoma lakes was measured in mid-August 2009 for comparison to boreal yedoma lakes. The Alaska lake data, collected in July and August 1997 and July 2009, were made available ref. 60 and G. Kling (personal communication, 10 April 2013). Relatively high nitrogen and phosphorus concentrations in the boreal yedoma thermokarst lakes (Extended Data Figs 3 and 4) are attributed to the release of nutrients from thawing yedoma surrounding lakes. This hypothesis is supported by soil and vegetation analyses in yedoma and non-yedoma surface types (Supplementary Information section 1.8).

31. Walter Anthony, K. M. & Anthony, P. Constraining spatial variability of methane ebullition in thermokarst lakes using point-process models. *J. Geophys. Res.* **118,** http://dx.doi.org/doi:10.1002/jgrg.20087 (2013).
32. Czudek, T. & Demek, J. Thermokarst in Siberia and its influence on the development of lowland relief. *Quat. Res.* **1,** 103–120 (1970).
33. Soloviev, P. A. Thermokarst phenomena and landforms due to frost heaving in Central Yakutia. *Biuletyn Peryglacjalny* **23,** 135–155 (1973).
34. Brouchkov, A., Fukuda, M., Fedorov, A., Konstantinov, P. & Iwahana, G. Thermokarst as a short-term permafrost disturbance, Central Yakutia. *Permafrost Periglacial Process.* **15,** 81–87 (2004).
35. Ferland, M. E., del Giorgio, P. A., Teodoru, C. R. & Prairie, Y. T. Long-term C accumulation and total C stocks in boreal lakes in northern Québec. *Glob. Biogeochem. Cycles* **26,** GB0E04 (2012).
36. Engstrom, D. R. & Rose, N. L. A whole-basin, mass balance approach to paleolimnology. *J. Paleolimnol.* **49,** 333–347 (2013).
37. Anderson, N. J., Dietz, R. D. & Engstrom, D. R. Land-use change, not climate, controls organic carbon burial in lakes. *Proc. R. Soc. Lond. B* **280,** 20131278 (2013).
38. Dean, W. E. Determination of carbonate and organic matter in calcareous sediments and sedimentary rocks by loss on ignition: comparison with other methods. *J. Sedim. Petrol.* **44,** 242–248 (1974).
39. Bundy, L. G. & Bremner, J. M. A simple titrimetric method for determination of inorganic carbon in soils. *Soil Sci. Soc. Am. J.* **36,** 273–275 (1972).
40. Reimer, P. J. *et al.* IntCal09 and Marine09 radiocarbon age calibration curves, 0–50,000 years cal BP. *Radiocarbon* **51,** 1111–1150 (2009).
41. Romanovskii, N. N. *Fundamentals of Cryogenesis of Lithosphere* 296–313 (Moscow Univ. Press, 1993).
42. Jorgenson, M. T. *et al.* Permafrost characteristics of Alaska. *Proc. Ninth Intl Conf. Permafrost* **3,** 121–122 (2008).
43. Grosse, G., Schirrmeister, L., Kunitsky, V. V. & Hubberten, H. W. The use of CORONA images in remote sensing of periglacial geomorphology: an illustration from the NE Siberian Coast. *Permafrost Periglacial Process.* **16,** 163–172 (2005).

44. Grosse, G., Schirrmeister, L. & Malthus, T. J. Application of Landsat-7 satellite data and a DEM for the quantification of thermokarst-affected terrain types in the periglacial Lena-Anabar coastal lowland. *Polar Res.* **25,** 51–67 (2006).
45. Veremeeva, A. & Gubin, S. Modern tundra landscapes of the Kolyma Lowland and their evolution in the Holocene. *Permafrost Periglacial Process.* **20,** 399–406 (2009).
46. Morgenstern, A., Grosse, G., Günther, F., Fedorova, I. & Schirrmeister, L. Spatial analyses of thermokarst lakes and basins in Yedoma landscapes of the Lena Delta. *Cryosphere* **5,** 849–867 (2011).
47. Morgenstern, A. Thermokarst and Thermal Erosion: Degradation of Siberian Ice-rich Permafrost. http://opus.kobv.de/ubp/volltexte/2012/6207/, PhD thesis, Potsdam Univ. (2012).
48. Grosse, G. *et al.* Distribution of late Pleistocene ice-rich syngenetic permafrost of the Yedoma Suite in East and Central Siberia, Russia. *USGS Open-file Rep.* 2013-1078 (2013).
49. Walker, D. A. *et al.* The Circumpolar Arctic vegetation map. *J. Veg. Sci.* **16,** 267–282 (2005).
50. Vtyurin, B. I. *Underground Ices of the USSR* [in Russian] 1–212 (Science, 1975).
51. Péwé, T. L., Journaux, A. & Stuckenrath, R. Radiocarbon dates and late-Quaternary stratigraphy from Mamontova Gora, unglaciated central Yakutia, Siberia, U.S.S.R. *Quat. Res.* **8,** 51–63 (1977).
52. Sher, A. V. *et al. Late Cenozoic of the Kolyma Lowland: XIV Pacific Science Congress, Tour Guide XI (Khabarovsk August 1979)* 1–116 (Academy of Sciences of the USSR, 1979).
53. Tomirdiaro, S. V. *Loess-ice Formation of Eastern Siberia in the Late Pleistocene and Holocene* 1–184 (Nauka, 1980).
54. Vasil'cuk, Y. K. *Oxygen Isotope Composition of Ground Ice Application to Paleogeocryological Reconstructions* [in Russian] Vols 1 and 2 (Russian Academy of Sciences and Lomonosov's Moscow University Publications, 1992).
55. Nikolaev, V. I., Mikhalev, D. V., Romanenko, F. A. & Brilli, M. Reconstruction of the conditions for North-East Russia permafrost formation on the isotope study results of Kolyma lowland key sections. [in Russian] *Ice Snow* **4,** 79–90 (2010).
56. Kanevskiy, M., Shur, Y., Fortier, D., Jorgenson, M. T. & Stephani, E. Cryostratigraphy of late Pleistocene syngenetic permafrost (yedoma) in northern Alaska, Itkillik River exposure. *Quat. Res.* (2011).
57. Schirrmeister, L., Siegert, C., Kunitzky, V. V., Grootes, P. M. & Erlenkeuser, H. Late Quaternary ice-rich permafrost sequences as a paleoenvironmental archive for the Laptev Sea Region in northern Siberia. *Int. J. Earth Sci.* **91,** 154–167 (2002).
58. Schirrmeister, L. *et al.* Periglacial landscape evolution and environmental changes of Arctic lowland areas for the last 60,000 years (western Laptev Sea coast, Cape Mamontov Klyk). *Polar Res.* **27,** 249–272 (2008).
59. Andreev, A. A. *et al.* Weichselian and Holocene palaeoenvironmental history of the Bol'shoy Lyakhovsky Island, New Siberian Archipelago, Arctic Siberia. *Boreas* **38,** 72–110 (2009).
60. Giblin, A., Luecke, C. & Kling, G. *Physical and Chemical Data for Various Lakes near Toolik Research Station, Arctic LTER Summer 2009* Arctic Long-Term Ecological Research Database, http://dx.doi.org/10.6073/pasta/1b77f4c8d8cc250ce0f90bbb17d9c976 (2009).
61. Lyons, W. B. & Finlay, J. C. in *Polar Lakes and Rivers: Limnology of Arctic and Antarctic Aquatic Ecosystems* (eds Vincent, W. F. & Laybourn-Parry, J.) 137–156 (Oxford Univ. Press, 2008).
62. Wetzel, R. G. & Likens, G. E. *Limnological Analyses* 3rd edn, 1–429 (Springer, 2000).
63. R Development Core Team. *R: A Language and Environment for Statistical Computing* http://www.R-project.org (R Foundation for Statistical Computing, 2009).
64. Kholodov, A. L. *et al.* Estimation of the organic carbon input to the arctic ocean due to erosion of Laptev and East-Siberian seashore. *Earth Cryosphere* **7,** 3–12 (2003).
65. Schirrmeister, L. *et al.* Periglacial landscape evolution and environmental changes of Arctic lowland areas for the last 60,000 years (western Laptev Sea coast, Cape Mamontov Klyk). *Polar Res.* **27,** 249–272 (2008).
66. Schneider, J., Grosse, G. & Wagner, D. Land cover classification of tundra environments in the Arctic Lena Delta based on Landsat 7 ETM+ data and its application for upscaling of methane emissions. *Remote Sens. Environ.* **113,** 380–391 (2009).
67. Hopkins, D. M. & Kidd, J. G. in *Proc. Fifth Intl Conf. Permafrost* (ed. Senneset, K.) 790–795 (Academic, 1988).
68. Jones, M. C., Grosse, G., Jones, B. M. & Walter Anthony, K. Peat accumulation in drained thermokarst lake basins in continuous, ice-rich permafrost, northern Seward Peninsula, Alaska. *J. Geophys. Res.* **117,** G00M07 (2012).
69. Kessler, M. A., Plug, L. J. & Walter Anthony, K. M. Simulating the decadal- to millennial-scale dynamics of morphology and sequestered carbon mobilization of two thermokarst lakes in NW Alaska. *J. Geophys. Res.* **117,** G00M06 (2012).
70. Ramaswamy, V. *et al.* in *Climate Change 2001: The Scientific Basis. Contribution of Working Group I to the Third Assessment Report of the Intergovernmental Panel on Climate Change* (eds Houghton, J. T. *et al.*) 350–416 (Cambridge Univ. Press, 2001).
71. Joos, F. *et al.* An efficient and accurate representation of complex oceanic and biospheric models of anthropogenic carbon uptake. *Tellus* **48,** 397–417 (1996).
72. Prather, M. *et al.* in *Climate Change 2001: The Scientific Basis. Contribution of Working Group I to the Third Assessment Report of the Intergovernmental Panel on Climate Change* (eds Houghton, J. T. *et al.*) 239–287 (Cambridge Univ. Press, 2001).
73. Walker, D. A. & Everett, K. R. Loess ecosystems of northern Alaska: regional gradient and toposequence at Prudhoe Bay. *Ecol. Monogr.* **61,** 437–464 (1991).
74. Weintraub, M. N. in *Phosphorus in Action, Soil Biology* (eds Bunemann, E. K. *et al.*) Ch. 12, 295–316 (Springer, 2011).

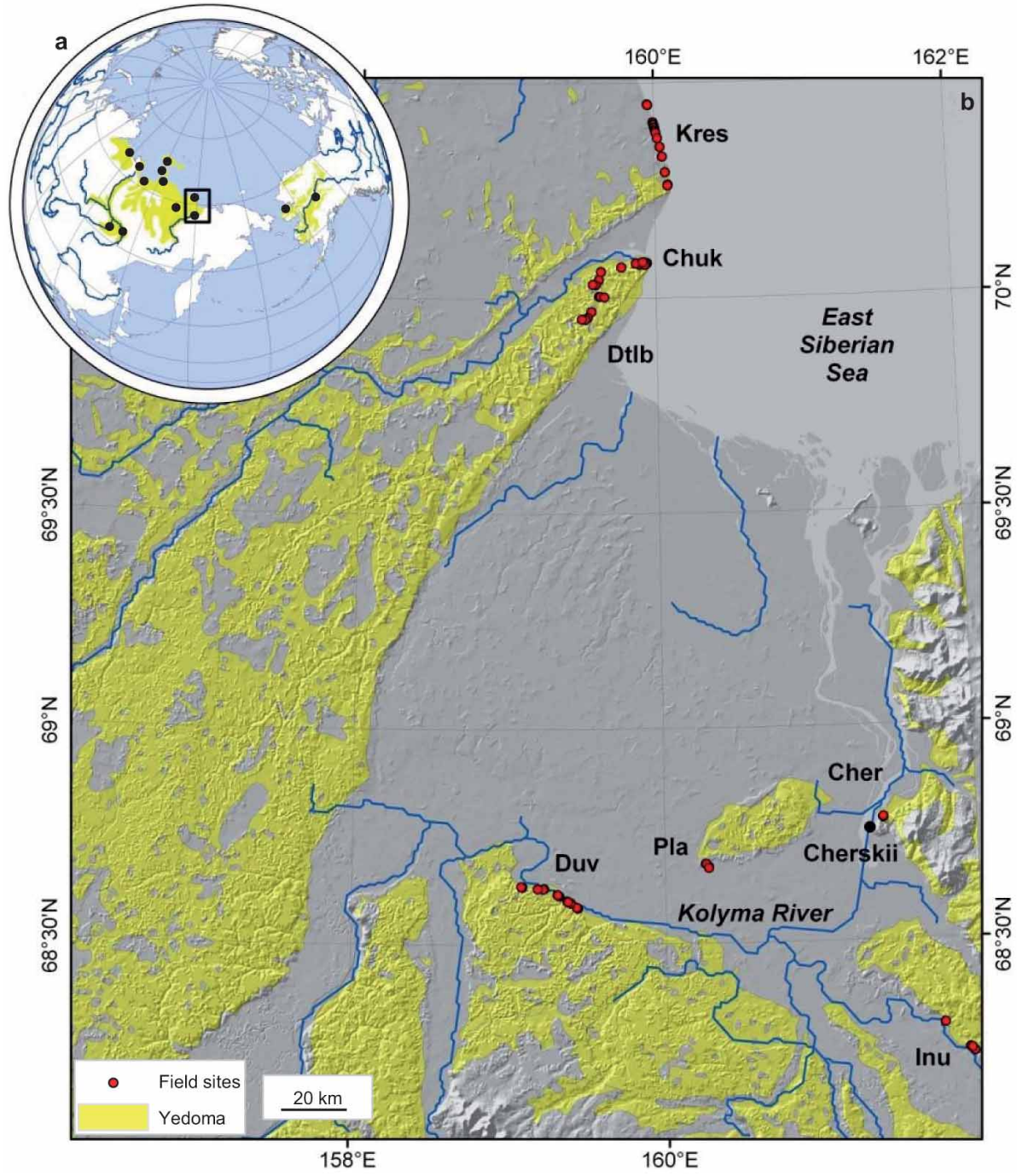

Extended Data Figure 1 | Map of main distribution of yedoma in the Beringia region in Siberia and Alaska (yellow regions). **a**, The Kolyma Lowland, considered largely covered by yedoma during the Last Glacial Maximum, now has only discontinuous yedoma coverage (yellow regions in **b**) owing to widespread destructive thermokarst and fluvial processes shaping the yedoma landscape since the early Holocene* (Supplementary Information section 1.1). Red dots in **b** indicate the locations of permafrost exposures sampled in boreal regions—Anuiy (Inu), Duvanii Yar (Duv), Plakhanski Yar (Pla), Cherskii (Cher)—and tundra regions—Chukochi Cape (Chuk and Dtlb) and Krestovskiy Cape (Kres). Literature data were synthesized from other western and eastern yedoma regions in Siberia[5,10,32,50–55,57–59,64–66] and Alaska[4,56,67–69], respectively (black dots in **a**). For map clarity, abundant lakes in the study regions were not plotted. **b**, Our central Beringia study region in the Kolyma Lowland in Northeast Siberia (small black frame in **a**; 60,000 km^2) is characterized by yedoma hills, deep yedoma lake basins, and fluvial flood plains of the Kolyma River and its tributaries.

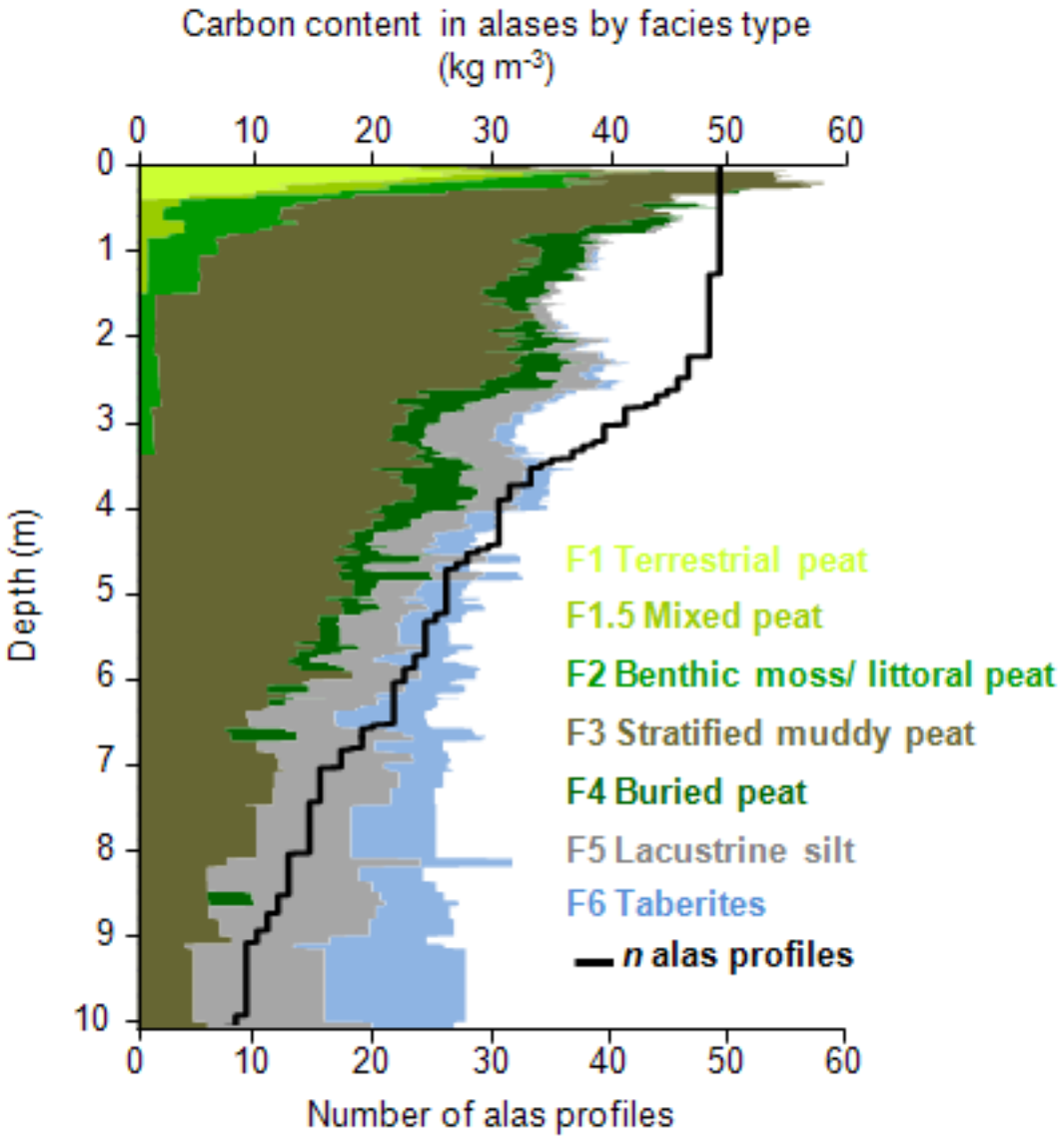

Extended Data Figure 2 | Relative contributions of facies F1–F6 to the average organic carbon content within the surface 10 m of North Siberian alases. The black line indicates the number of exposure profiles included in the observations. Extrapolating the Holocene* organic carbon component observed in these profiles to the extent of deep thermokarst basins in the yedoma region of Beringia (925,400 km^2, Supplementary Information section 1.6.1), we estimate the following Holocene* carbon pool sizes in the alases: 12 ± 2.5 Pg for 0–0.3 m, 36 ± 4.1 Pg for 0–1 m, 64 ± 4.3 Pg for 0–2 m, 89 ± 6.6 Pg for 0–3 m, 126 ± 9.0 Pg for 0–5 m, 144 ± 10.1 Pg for 0–7 m and 155 ± 11.6 Pg for 0–10 m. Error terms represent standard error at the 95% confidence limits derived by propagating uncertainties of the estimates of mean organic carbon bulk density for each depth interval, based on the interval size and number of field samples measured; additional uncertainty associated with the yedoma region extent is shown in Extended Data Table 3. Below 10 m, extrapolating our observation of Holocene* carbon in 7% of exposures, we estimate an additional 5 Pg C. Pleistocene carbon, also observed in the profiles and included in this figure, is accounted for in the regional-scale carbon mass balance calculation since these deposits extended deeper than we were able to expose in cross-section (Methods).

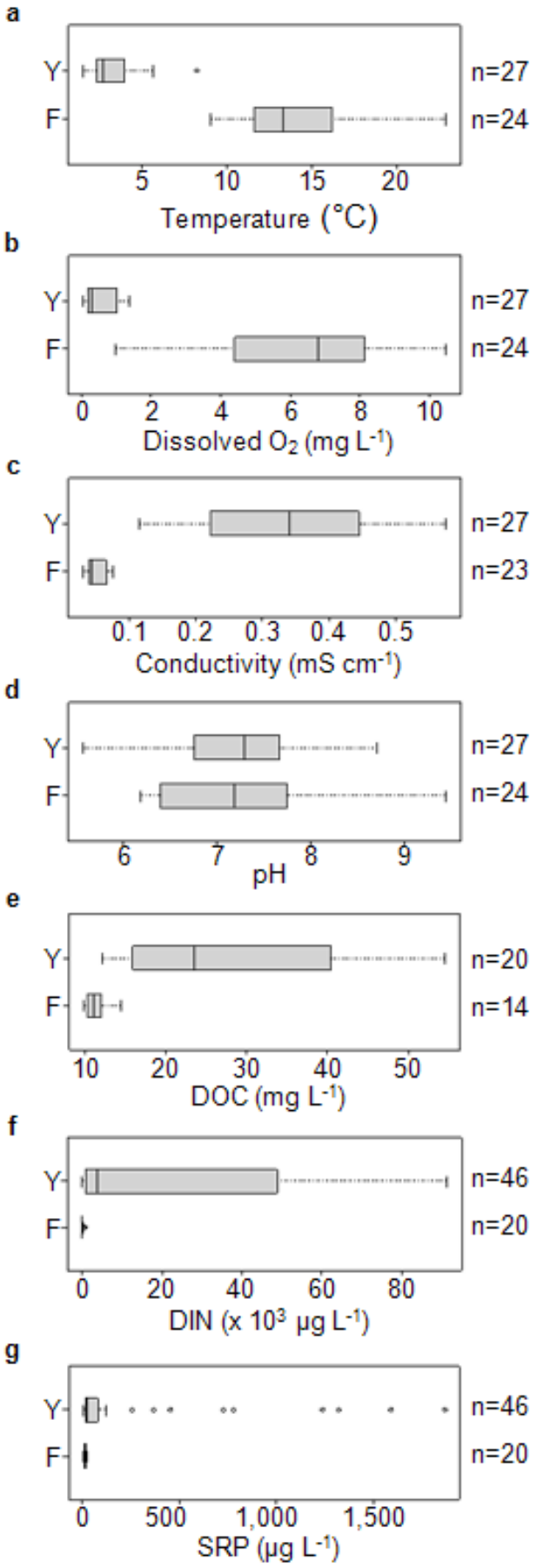

Extended Data Figure 3 | Box plots showing physiochemical characteristics of lake bottom water in thermokarst lakes formed in Pleistocene yedoma (Y) and non-yedoma Holocene floodplain (F) permafrost in the same region of North Siberia. DOC, dissolved organic carbon; DIN, dissolved inorganic nitrogen, dominated by ammonium; SRP, soluble reactive phosphorus. 'Conductivity' means specific conductivity. The number of samples *n* represent single observations per lake per day on different dates during June, July and August 2002–2003 from 9 yedoma and 13 floodplain thermokarst lakes (see Methods). The two-sample, two-sided Mann–Whitney test revealed differences between Y and F for all parameters except pH ($P < 0.01$).

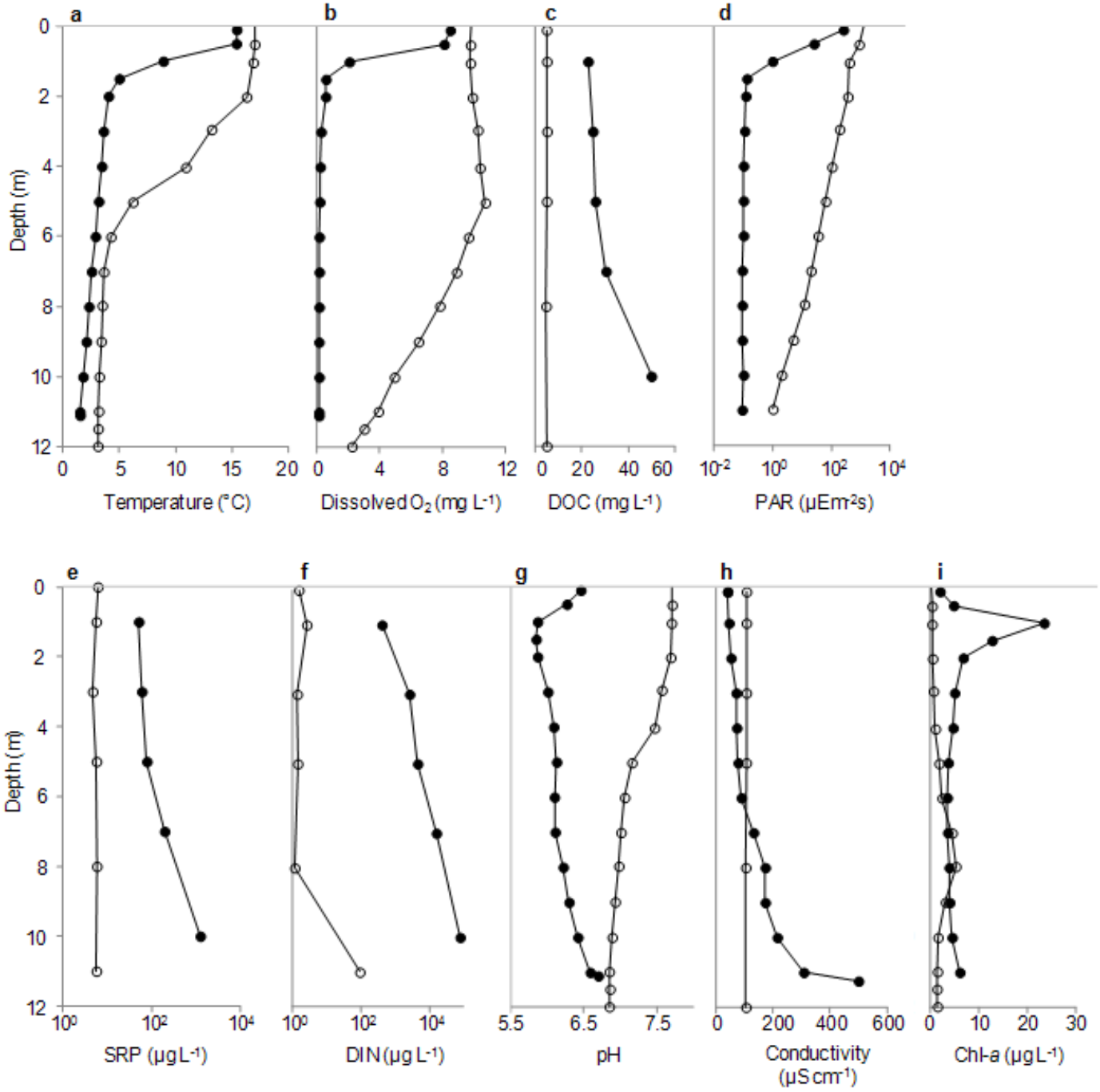

Extended Data Figure 4 | Comparison of physical, chemical, and biological characteristics of a yedoma lake and a non-yedoma lake of similar depth, volume and latitude in midsummer. Closed circles indicate the yedoma lake, Grass Lake (68.75° N, 161.38° W), near Cherskii, Russia. Open circles indicate the non-yedoma lake (68.64 °N, −149.61 °W) near Toolik Field Station, Alaska, USA. Both lakes were thermally stratified, but the yedoma lake had an anaerobic hypolimnion with exceedingly high concentrations of DOC, SRP, DIN and other solutes (indicated by specific conductivity). In addition, the yedoma lake had a much lower light environment, a colder lake bottom temperature, lower pH, and relatively high concentrations of chlorophyll-*a* in the epilimnion and dissolved ions in the hypolimnion. The Toolik Field Station data were from ref. 60 and G. Kling (personal communication, 10 April 2013).

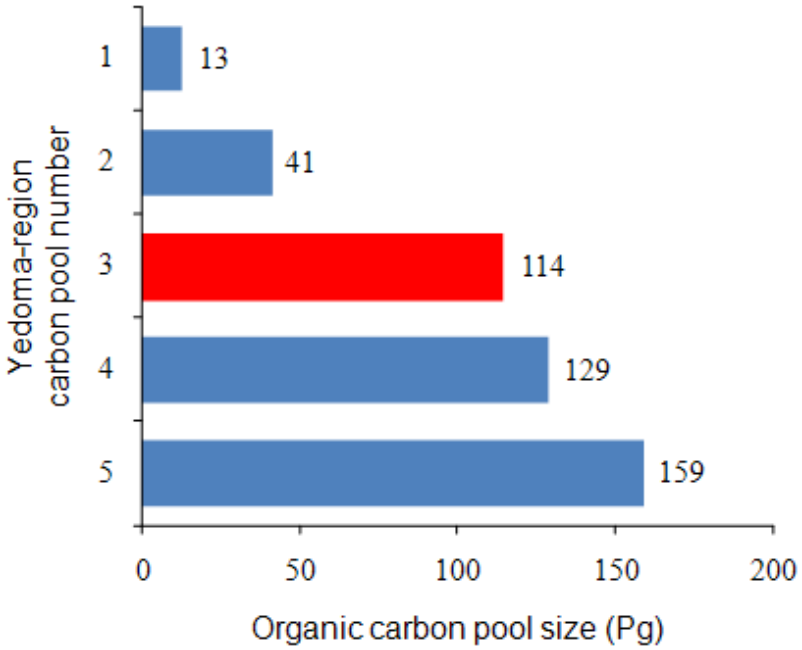

Extended Data Figure 5 | Organic carbon pools in the yedoma region. Our yedoma-region total organic carbon pool-size estimate (456 ± 45 Pg; Extended Data Table 3) is the sum of the following subset pools: (1) Holocene peat located above undisturbed yedoma permafrost; (2) yedoma that thawed, was reworked, and is now stored in thermokarst basins in facies F3 and F5; (3) taberite sediments representing *in situ* thawed, diagenetically altered yedoma in facies F6; (4) undisturbed yedoma in facies F7; (5) non-yedoma, Holocene* carbon stored in thermokarst basins in facies F1–F5 that was fixed via photosynthesis in and around the basins. Taberite deposits (red bar) are an important component of the yedoma-region total carbon pool that were not included in the recent yedoma-region carbon inventory of ref. 11.

Extended Data Table 1 | Physical and chemical characteristics of facies in North Siberian permafrost exposures

Facies	Moisture content (%) mean ± s.e., *n*	Dry bulk density (g soil cm^{-3}) mean ± s.e., *n*	Inorganic C content (%) mean ± s.e., *n*	Organic matter content (%) mean ± s.e., *n*	Thickness[a] (m) mean ± s.e., *n*	Thickness[b] (m) mean ± s.e., median, *n*	Age (Cal. Yr. BP) mean ± s.e., *n*	median	(min to max)
F1	37 ± 4%, 14	0.21 ± 0.05, 14	0.96 ± 0.37%, 14	72 ± 4%, 21	0.13 ± 0.02, 49	0.17 ± 0.02, 0.15, 33	2,191 ± 1,770, n=4	642	(-2 to 7,479)
F1.5	39 ± 5%, 14	0.17 ± 0.02, 14	0.67 ± 0.13%, 14	70 ± 5%, 14	0.10 ± 0.04, 49	0.57 ± 0.13, 0.50, 9	3,734 ± 1,133, n=5	4,017	(699 to 6,523)
F2	82 ± 3%, 32	0.13 ± 0.02, 32	0.55 ± 0.16%, 32	82 ± 3%, 34	0.22 ± 0.08, 49	0.73 ± 0.21, 0.40, 15	4,368 ± 1,168,n= 9	3,533	(492 to 9,492)
F3	35 ± 1%, 132	1.05 ± 0.04, 132	0.97 ± 0.11%, 132	7.6 ± 0.5%, 249	3.11 ± 0.32, 49	3.62 ± 0.49, 2.46, 28	7,932 ± 693, n=23	8,613	(2,547 to 13,504)
F4	67 ± 4%, 20	0.39 ± 0.06, 40	0.92 ± 0.11%, 40	50 ± 4%, 67	0.20 ± 0.05, 49	0.24 ± 0.09, 0.05, 23	5,826 ± 923, n=16	5,038	(1,120 to 13,808)
F5	35 ± 2%, 61	1.09 ± 0.05, 61	0.83 ± 0.07%, 61	4.9 ± 0.2%, 80	1.12 ± 0.16, 49	1.62 ± 0.26, 0.80, 22	19,331 ± 7,318, n=5	15,331	(7,220 to 47,757)
F6	26 ± 1%, 14	1.35 ± 0.05, 14	1.01 ± 0.13%, 14	3.3 ± 0.1%, 40	-	-			
F7	31 ± 1%, 25	1.22 ± 0.05, 25	0.97 ± 0.07%, 25	4.4 ± 0.3%, 44	-	38.4 ± 1.8, 17†	n=4	>47,000	(42,319 to >47,000)

Shown are the facies gravimetric water content (percentage moisture), dry bulk density, inorganic carbon and organic matter contents, thickness, and maximum ^{14}C ages. We collected and analysed 595 samples among the permafrost exposures in alases and yedoma. At several exposure sites, the average of field triplicate samples of yedoma (F7) were used as $n = 1$ in calculation of regional-scale means and standard error in this table and Extended Data Table 2. The purpose of this table is to show the physical and chemical characteristics of the facies; the mean values presented here were not used in upscaling calculations of Holocene* carbon stocks (see Methods and Fig. 2e). Values in this table were used together with other literature data synthesis in mass balance calculations to determine Pleistocene carbon stocks, given that we did not reach the base of the Pleistocene-aged deposits, F6 and F7, by digging in our exposures (see Methods). Facies thickness is expressed as the mean and standard error among all 49 studied exposures, including thicknesses with a zero value for instances where facies were not observed (Thickness[a]). Thickness[b] is the mean and median thickness of each facies among exposures where the facies was observed. Macrofossil ages represent the average maximum ages of the facies (not the average age of facies) because we often sampled the lower sections of the facies to date events such as lake formation and drainage. The large variability in maximum ^{14}C ages within facies reflects lake formation at different times since the onset of the last deglaciation about 14 kyr ago; these ^{14}C data are used in this study as secondary independent evidence for Pleistocene versus Holocene* carbon fractions in facies (Supplementary Information section 1.4).

† Undisturbed yedoma thickness determined for a larger sample size from map-based analysis. Measured yedoma thicknesses at studied exposures was 31.5 ± 5.9 m ($n = 4$). Our carbon stock and pool size calculations (Extended Data Table 3) assume an average undisturbed yedoma deposit thickness of 25 ± 5 m, as determined from extensive literature[10,32,50–56].

Extended Data Table 2 | Organic carbon concentrations in yedoma (F7) and taberites (F6) and organic carbon bulk density from various subregions in North Siberia

	(a) Organic carbon content (%)						(b) Yedoma (F7) organic carbon bulk density (%)
	Yedoma (F7)			Taberites (F6)			
Subregion	Mean	s.e.	*n*	Mean	s.e.	*n*	Difference	(kg C m^{-3})
Chukochi Cape*	2.41 ±	0.22	17	1.76 ±	0.07	19	27%	27.88
Anuiy*	2.96 ±	0.74	7	2.16 ±	0.22	4	27%	30.75
Duvanni Yar*†	2.77 ±	0.39	8	1.98 ±	0.10	10	28%	24.62
Laptev Sea†	3.38 ±	0.17	468	2.70 ±	1.40	9	20%	
East Siberian/Laptev Seas‡	2.03 ±	0.13	24	1.29 ±	0.07	29	36%	
Plakhanski Yar*								26.66
Cape Mamontov Klyk†								24.84
Lena Delta†								30.32
Bykovsky Peninsula†								25.04
Bol'shoy Lyakhovsky Island†								17.72
Mean ± SE							28 ± 12%	25.98 ± 1.45

* Data collected by this study; †data from ref. 5; ‡data from ref. 64. **a**, The organic matter content of yedoma was significantly higher than that of taberites (two-way analysis of variance, ANOVA, $F = 8.12_{22,1}$, $P = 0.0061$) at the $\alpha = 0.05$ level. Interaction effects of facies by zone (boreal versus tundra) or facies by subregions listed in the table were not significant. This indicates that the organic matter contents of yedoma and taberites are statistically distinct irrespective of the subregion or zone in which they are measured. Across subregions, the organic matter content of yedoma was on average 28% higher than that of taberites (4%–52%, lower and upper 95% confidence interval). The large uncertainty in the mean difference between yedoma and taberite organic carbon concentration is largely due to unpaired sampling in the literature data sets († and ‡), which had different goals in their study designs. The more tightly constrained difference in our field data sets results from pair-wise sampling of adjacent yedoma/alas systems in our study, which was designed specifically to assess site-specific carbon loss. **b**, The yedoma organic carbon bulk density was calculated from field measurements in eight subregions of North Siberia. The value used for Duvanni Yar was the average of both independent studies. Values in this table do not account for ice-wedge volume.

Extended Data Table 3 | Calculations (a) and uncertainty analysis (b) of estimated carbon pool sizes and fluxes in the yedoma region

a

		Area	Cumulative loss to atmosphere		Export to sea	
Land cover class	Fraction	(10^6 km^2)	(kg C_P m^{-2})	(Pg C_P)	(kg C_P m^{-2})	(Pg C_P)
Total yedoma region	100%	1.322 ± 0.132†		100 ± 34‖		45 ± 12**
Undisturbed yedoma	30%	0.397 ± 0.040†				
Thermokarst lakes/ alases	55%	0.727 ± 0.073†	131 ± 45‡	95 ± 34¶		
Thermoerosional gullies	15%	0.198 ± 0.020†	27 ± 9§	5 ± 2#	227 ± 49☆	45 ± 12**

	Present-day stocks		Regional soil carbon pools			
Land cover class	(kg C_P m^{-2})	(kg C_H m^{-2})	(Pg C_P)	(Pg $C_{H\text{-}tk}$)	(Pg C_H)	(Pg C_{total})
Total yedoma region			284 ± 40¶¶	159 ± 24¶¶	172 ± 19¶¶	456 ± 45¶¶
Undisturbed yedoma	325 ± 69††		129 ± 30		13 ± 1##	142 ± 30
Thermokarst lakes/ alases	194 ± 30‡‡	172 ± 19‖‖	141 ± 26	125 ± 19	125 ± 19	266 ± 32
Thermoerosional gullies	70 ± 9§§	172 ± 19‖‖	14 ± 2	34 ± 5	34 ± 5	48 ± 6

b

			Loss to atmosphere	Export to sea	Regional soil carbon pools		
Uncertainty factor	Value used	Uncertainty	(Pg C_P)	(Pg C_P)	(Pg C_P)	(Pg $C_{H\text{-}tk}$)	(Pg C_{total})
Yedoma-region area	1.322 x 10^6 km^2 ± 10%	± 20%	100 ± 38	45 ± 16	284 ± 52	159 ± 36	456 ± 60
Pleistocene *vs*. Holocene* C attribution							
Fraction C_p decomposed (F3)	56 ± 24%	95 ± 0%	119 ± 33	-	265 ± 38	175 ± 26	453 ± 43
Fraction C_p decomposed (F5)	28 ± 12%	40 ± 0%	104 ± 30	-	280 ± 34	163 ± 24	456 ± 39
Thickness of F3 and F5	mean	median	96 ± 31	-	288 ± 41	-	460 ± 45
Holocene* carbon stocks in alases	mean	median	-	-	-	153 ± 23	450 ± 44
Woody biomass	2.3 kg C m^{-2}	0.7 kg C m^{-2} to	-	-	-	158 ± 24	455 ± 45
(forest succession & density)		5.1 kg C m^{-2}				161 ± 24	458 ± 45
Woody biomass extent	0.889 x 10^6 km^2	+47%	-	-	-	160 ± 24	457 ± 45
(boreal *vs*. boreal + tundra zones)							
Thermokarst-affected area	70%	-7% to	93 ± 32	42 ± 11	294 ± 43	148 ± 22	457 ± 47
(percent of region)		+11%	112 ± 38	50 ± 13	267 ± 37	177 ± 27	454 ± 43

We included present-day carbon stocks, regional soil carbon pools for different landscape cover classes of the yedoma region (undisturbed yedoma, thermokarst lakes and alases, and thermoerosional gullies) and cumulative carbon export to the atmosphere or sea. Pleistocene yedoma-derived carbon is indicated as C_p; Holocene* carbon is C_H. The regional soil carbon pool $C_{H\text{-}tk}$ specifies Holocene* carbon in thermokarst basins only, while C_H includes also the Holocene surface soil overlying undisturbed yedoma. Uncertainties are represented as propagated standard errors unless otherwise noted. In **b**, '-' indicates that an additional uncertainty had no impact on the calculation of a particular carbon pool. Uncertainty sources, conservative basis for assumptions, additional minor uncertainties, and impacts on upscaling results are discussed in Supplementary Information section 1.7.

† See Methods; the error term represents 10% uncertainty (Supplementary Information section 1.7.3).

‡ 131 ± 76 kg C_p m^{-2} (lost to the atmosphere from thermokarst lakes as methane and carbon dioxide) = 325 ± 69 kg C_p m^{-2} (yedoma carbon stock, see ††) minus 194 ± 30 kg C_p m^{-2} (C_p remaining in lake basins, see ‡‡).

§ 27 ± 9 kg C_p m^{-2} (lost to the atmosphere from thermoerosional gullies as methane and carbon dioxide) = 325 ± 69 kg C_p m^{-2} (yedoma carbon stock, see ††) minus 70 ± 9 kg C_p m^{-2} (C_p remaining in lake basins, see §§) minus 227 ± 49 kg C_P m^{-2} (C_p exported to sea, see ☆); this assumes 28 ± 12% of the remaining thawed yedoma organic carbon decomposed under anaerobic conditions in F5 and F6, forming methane and carbon dioxide that escaped to the atmosphere (see Extended Data Table 2 and Supplementary Information section 1.4).

‖ 100 ± 56 Pg C_p (total Pleistocene yedoma carbon lost to the atmosphere as CH_4 and CO_2) = 95 ± 56 Pg C_p (loss from thermokarst lakes, see ¶) plus 5 ± 2 Pg C_p (loss from thermoerosional gullies, see #).

¶ 95 ± 56 Pg (C_p lost to the atmosphere as methane and carbon dioxide from thermokarst lakes) = 131 ± 76 kg C_p m^{-2} (see ‡) times 727,100 ± 72,700 km^2 (thermokarst lake/alas area, see †).

5 ± 2 (C_p lost to the atmosphere as methane and carbon dioxide from thermoerosional gullies) = 27 ± 9 kg C_p m^{-2} (see §) times 198,300 ± 19,800 km^2 (thermoerosional gully area, see †).

☆ 227 ± 49 kg C_P m^{-2} (thawed Pleistocene yedoma carbon exported to the sea, including river deltas and continental shelves) = 0.7 (eroded fraction; Supplementary Information section 1.5) times 325 ± 69 kg C_p m^{-2} (yedoma carbon stock, see ††).

** 45 ± 12 Pg (C_p exported to sea) = 227 ± 49 kg C_p m^{-2} (see ☆) times 198,300 ± 19,800 km^2 (thermoerosional gully area, see †).

†† 325 ± 69 kg C_p m^{-2} (original, undisturbed yedoma carbon stock) = 25.98 ± 1.45 kg C_p m^{-3} (Extended Data Table 2) × 25 ± 5 m yedoma deposit thickness × 50% ± 3% ice wedges (Methods).

‡‡ 194 ± 30 kg C_P m^{-2} (Pleistocene yedoma-derived carbon remaining in alases) = 29 ± 16 kg C_P m^{-2} (in facies F3) + 22 ± 4 kg C_P m^{-2} (in facies F5) + 143 ± 25 kg C_P m^{-2} (in facies F6). Assumes 28% ± 12% of original yedoma organic carbon decomposed under anaerobic conditions in F5 and F6, and 56% ± 24% under aerobic and anaerobic conditions in F3, forming methane and carbon dioxide that escaped to the atmosphere (see Extended Data Table 2 and Supplementary Information section 1.4). Calculation of the mineral fraction thickness of F3 and F5, based on dry bulk density mixing ratios, is summarized in equations (1) and (2) (Supplementary Information section 1.4). We determined the mean thickness of F6 based on a conservation of mass of yedoma on the landscape, accounting for the difference in dry bulk density between frozen (F7) and thawed yedoma (F6).

§§ 70 ± 9 kg C_P m^{-2} (Pleistocene yedoma-derived carbon remaining in thermoerosional gullies) = 22 ± 4 kg C_P m^{-2} (in facies F5) + 48 ± 9 kg C_P m^{-2} (in facies F6). Assumes 28% ± 12% of original yedoma organic carbon decomposed under anaerobic conditions in F5 and F6, and 56% ± 24% under aerobic and anaerobic conditions in F3, forming methane and carbon dioxide that escaped to the atmosphere (see Extended Data Table 2 and Supplementary Information section 1.4).

‖‖ 172 ± 19 kg C_H m^{-2} is the area-weighted average (32% tundra, 68% boreal) of Holocene* organic carbon stocks in tundra alases (122 ± 16 kg C m^{-2}, n = 18 sites) and boreal alases (196 ± 27 kg C m^{-2}, n = 10 sites) (Fig. 2e).

¶¶ The regional soil carbon pools are the sum of the Pleistocene yedoma-derived and/or Holocene* carbon pools in each of the land cover classes (undisturbed yedoma, thermokarst lakes/alases, and thermoerosional gullies). The carbon pools within each land cover class were calculated as the product of the associated carbon stocks and cover class areas.

13 ± 1 kg C_H m^{-2} is the surface soil (0–100 cm) Holocene organic carbon pool overlying upland yedoma estimated from the distribution of histels, orthels and turbels in the Northern Circumpolar Soil Carbon Database (NCSCD)[13] (Supplementary Information section 3.5). The error term is a minimum estimate, representing the 10% uncertainty in the yedoma region extent (this study, Supplementary Information section 1.7.3); errors associated with the NCSCD carbon stocks are unknown.

Extended Data Table 4 | Greenhouse gas parameters for atmospheric model

Gas	Index, i	A_i * (10^{-13} W m^{-2} kg^{-1})	f_i †	τ_i ‡ (yr)	ε_i *
CO_2	0	0.0198	0.176	*infinite* §	1
	1	0.0198	0.138	421	1
	2	0.0198	0.186	70.6	1
	3	0.0198	0.242	21.4	1
	4	0.0198	0.259	3.42	1
CH_4	5	1.3	1	12.0	1.3

See equation (3) and Supplementary Information section 1.6.6.
* Ref. 70.
† Ref. 71.
‡ CO_2 values from ref. 71; CH_4 value from ref. 72.
§ Modelled as 10^8 yr.

Extended Data Table 5 | Mean nitrogen (N) and phosphorus (P) concentrations in ice wedges, soils and present-day vegetation

Pool	Element	Yedoma upland		Floodplain	P-value
Ice wedges					
(ppm)	Total N	1.79		-	
(mg L^{-1})	Total dissolved P	0.29		-	
Soil soluble (g/m^2)	N	2.43	=	2.28	--
	P	1.27	>	0.18	***
	N:P	2.21	<	12.5	***
Soil bulk (g/m^2)	N	222	<	494	***
	P	39	<	63	***
	N:P	6	=	6	--
Salix foliage (%)	N	2.07	=	2	--
	P	0.3	<	0.42	**
	C:N	24	=	25	--
	N:P	7.3	>	5.8	*
Salix litter (%)	N	0.71	<	0.94	**
	P	0.21	>	0.09	***
	C:N	64	>	50	*
	N:P	3.79	<	10.82	***
	% N retranslocated	67	=	64	--
	% P retranslocated	30	<	80	***
	N:P retranslocated	2.2	>	0.8	***
Salix litter soluble (mg/g)	C	8.9	>	5.8	*
	N	0.83	>	0.71	*
	P	2.29	>	0.55	***
	C:N	115	>	90	*
	N:P	0.44	<	1.5	**
	% mass lost	26	>	15	*
Benthic brown moss (%)	N	1.95		-	
	P	0.12		-	
	N:P	20.37		-	

Results are shown for active layer soil and shrubs for two permafrost-dominated landscape positions near Cherskii in northeast Siberia (Pleistocene yedoma upland and Holocene floodplain), and mean N and P for Pleistocene-aged yedoma ice wedges and yedoma thermokarst-lake mosses. Means are for $n = 4$ terrestrial sites on the Holocene floodplain, $n = 6$ sites terrestrial sites in the Pleistocene yedoma upland, $n = 6$ yedoma ice wedges, and $n = 11$ mosses from eight yedoma thermokarst lakes. *P* values are from Mann–Whitney U tests. Significant differences at $^*P < 0.05$, $^{**}P < 0.01$ and $^{***}P < 0.001$. Results for *Salix* (willow) are used to illustrate contrasts in litter nutrient retention between landscapes because it was common in both environments. Phosphorus retranslocation was significantly lower for yedoma upland versus floodplain plants ($P < 0.01$), while N retranslocation was highest in the yedoma upland. Higher N than P retranslocation together with higher soil P availability suggests that P is available in excess of N on the yedoma upland. Bulk N and P concentrations of yedoma were similar to other arctic soils[73,74], but high soil P availability, low plant P retranslocation, and high aquatic P concentrations support the idea that yedoma soils have very high bioavailable P pools. High litter P concentration and high litter soluble P pools also indicate high P availability for leaching and runoff to lakes. Further evidence for high P mobility in yedoma soils is that the yedoma thermokarst-lake P concentrations (Extended Data Figs 3 and 4) are much higher than in other arctic lakes in Alaska and Canada[61]. Phosphorus and nitrogen concentrations in benthic mosses of yedoma thermokarst lakes (*Warnstorfia fluitans*, *W. exannulatus*, *D. anduncus*, *D. vernicosis*, *Scorpidium revolvens*, *S. scorpiodes*, *Calliergon giganteum*) were also well above critical concentrations (about 0.09% P, about 1% N)[20].